The Astrophysical Journal, 667:176–190, 2007 September 20

THE SLOAN LENS ACS SURVEY. IV. THE MASS DENSITY PROFILE OF EARLY-TYPE GALAXIES OUT TO 100 EFFECTIVE RADII

Raphaël Gavazzi,[1] Tommaso Treu,[1] Jason D. Rhodes,[2,3] Léon V. E. Koopmans,[4] Adam S. Bolton,[5] Scott Burles,[6] Richard J. Massey,[3] and Leonidas A. Moustakas[2]

Received 2007 January 18; accepted 2007 April 17

ABSTRACT

We present a weak-lensing analysis of 22 early-type (strong) lens galaxies, based on deep *HST* images obtained as part of the Sloan Lens ACS Survey. Using advanced techniques to control systematic uncertainties, we show that weak-lensing signal is detected out to $\sim 300\ h^{-1}$ kpc (at the mean lens redshift $z = 0.2$). We analyze blank control fields from COSMOS in the same manner, inferring that the residual systematic uncertainty in the tangential shear is less than 0.3%. A joint strong- and weak-lensing analysis shows that the average *total* mass density profile is consistent with isothermal (i.e., $\rho \propto r^{-2}$) over two decades in radius (3–300 h^{-1} kpc, approximately 1–100 effective radii). This finding extends by over an order of magnitude in radius previous results, based on strong lensing and/or stellar dynamics, that luminous and dark components "conspire" to form an isothermal mass distribution. In order to disentangle the contributions of luminous and dark matter, we fit a two-component mass model (de Vaucouleurs+NFW) to the weak- and strong-lensing constraints. It provides a good fit to the data with only two free parameters: (1) the average stellar mass-to-light ratio $M_*/L_V = 4.48 \pm 0.46\ h\ M_\odot\ L_\odot^{-1}$ (at $z = 0.2$), in agreement with that expected for an old stellar population; (2) the average virial mass-to-light ratio $M_{\rm vir}/L_V = 246^{+101}_{-87}\ h\ M_\odot\ L_\odot^{-1}$. Taking into account the scatter in the mass-luminosity relation, the latter result is in good agreement with semianalytical models of massive galaxy formation. The dark matter fraction inside the sphere of radius, the effective radius, is found to be 27% ± 4%. Our results are consistent with galaxy-galaxy lensing studies of early-type galaxies that are not strong lenses, in the 30–300 h^{-1} kpc radius range. Thus, within the uncertainties, our results are representative of early-type galaxies in general.

Subject headings: dark matter — galaxies: elliptical and lenticular, cD — galaxies: structure — gravitational lensing

Online material: color figures

1. INTRODUCTION

It is now commonly accepted that cold nonbaryonic dark matter (DM) dominates the dynamics of the universe. Whereas the so-called ΛCDM (cold dark matter) paradigm has been remarkably successful at reproducing with high level of precision the properties of the universe on scales larger than Mpc (e.g., Spergel et al. 2007; Tegmark et al. 2004; Seljak et al. 2005), the situation at galactic and subgalactic scales is more uncertain. DM-only numerical simulations make very clear predictions. DM halos have a characteristically "cuspy" radial profile (e.g., Navarro et al. 1997, 2004; Moore et al. 1998; Ghigna et al. 1998; Jing 2000; Stoehr et al. 2002), are triaxial (Jing 2002; Kazantzidis et al. 2004; Hayashi et al. 2007), and have abundant substructure (e.g., Moore et al. 1999; De Lucia et al. 2004; Gao et al. 2004; Taylor & Babul 2004). From an observational point of view, substantial effort has been devoted to comparing those predictions to observations with debated results in the case, e.g., of low surface brightness galaxies (Salucci 2001; de Blok et al. 2003; Swaters et al. 2003; Gentile et al. 2004; Simon et al. 2005) or at galaxy cluster scales (e.g., Sand et al. 2004; Gavazzi 2005; Comerford et al. 2006). The main source of ambiguity in such comparisons is due to the effects of baryons. Although a minority in terms of total mass, baryons are dissipative and spatially more concentrated than the DM, playing a critical role at scales below tens of kiloparsecs. Understanding baryonic physics and the interplay between dark and luminous matter is necessary to understand how galaxies form and, ultimately, to test the cosmological model. From an observational point of view, measuring the relative spatial distribution of stars, gas, and DM is essential to provide clues to help understand the physical processes and hard numbers to perform quantitative tests of models.

The dark halos of early-type (i.e., elliptical and lenticular) galaxies have been particularly hard to detect and study, due to the general lack of kinematic tracers, such as H I, at large radii. Studies of local galaxies based on stellar kinematics (Bertin et al. 1994; Gerhard et al. 2001; Mamon & Łokas 2005a, 2005b; Cappellari et al. 2006), kinematics of planetary nebulae (Romanowsky et al. 2003; Arnaboldi et al. 2004; Merrett et al. 2006), and temperature profile of X-ray–emitting plasma (Humphrey et al. 2006) indicate that at least for the most massive systems DM halos are generally present. The total mass density profile is found to be close to isothermal ($\rho_{\rm tot} \propto r^{-2}$) on scales out to a few effective radii.

In the distant universe an additional mass tracer is provided by gravitational lensing. At scales comparable to the effective radius, strong gravitational lensing makes it possible to detect and study the mass profile and shape of individual halos (Kochanek 1995) or statistically of a population of halos (Rusin et al. 2003). The combination of strong lensing with stellar kinematics (Treu & Koopmans 2002, 2004; Koopmans & Treu 2002, 2003; Koopmans et al. 2006) is particularly effective and allows one to decompose

[1] Department of Physics, University of California, Santa Barbara, CA 93106-9530.
[2] Jet Propulsion Laboratory, California Institute of Technology, Pasadena, CA 91109.
[3] California Institute of Technology, Pasadena, CA 91125.
[4] Kapteyn Astronomical Institute, University of Groningen, 9700 AV Groningen, Netherlands.
[5] Harvard-Smithsonian Center for Astrophysics, Cambridge, MA 02138.
[6] Department of Physics and Kavli Institute for Astrophysics and Space Research, Massachusetts Institute of Technology, Cambridge, MA 02139.

the total mass distribution into luminous and dark matter with good precision, yielding information on the internal structure of early-type galaxies all the way out to the most distant lenses known at $z \sim 1$. At larger scales, the surface mass density is too low to produce multiple images. However, the weak-lensing signal can be detected statistically by stacking multiple galaxies and measuring the distortion of the background galaxies. The statistical nature of this measurement imposes a certain degree of spatial smoothing or binning, which in turn limits the angular resolution of weak-lensing studies.

In this paper we exploit deep Advanced Camera for Surveys (ACS) images of 22 gravitational lenses from the Sloan Lens ACS (SLACS) Survey (Bolton et al. 2006; Treu et al. 2006a; Koopmans et al. 2006 hereafter Papers I, II, and III, respectively) to perform a joint weak- and strong-lensing analysis. This allows us to bridge the gap between the two regimes and study the mass density profile of early-type galaxies across the entire range ~1–100 effective radii, disentangling the luminous and dark components.

From a technical point of view, joint weak- and strong-lensing analysis has already been applied in the past to clusters of galaxies and galaxies in clusters (Natarajan & Kneib 1997; Geiger & Schneider 1998; Natarajan et al. 2002; Kneib et al. 2003; Gavazzi et al. 2003; Bradač et al. 2005a, 2005b). However, there are important differences with respect to galaxy scales. First and foremost, clusters produce a much stronger weak-lensing signal; therefore, it can be detected and studied for individual systems. Second, since clusters are spatially more extended than galaxies, relatively large smoothing scales can be adopted to average the signal over background galaxies. In contrast, the signal of individual galaxies is too "weak" to be detected, so that stacking a number of lens galaxies is required to reach a sufficient density of background sources. For this purpose, previous studies have typically relied on a very large sample of galaxies (Brainerd et al. 1996; Griffiths et al. 1996; Wilson et al. 2001; Guzik & Seljak 2002; Hoekstra et al. 2004, 2005; Kleinheinrich et al. 2006) or recently on the Sloan Digital Sky Survey (SDSS; Sheldon et al. 2004, hereafter S04; Mandelbaum et al. 2006, hereafter M06). As we show in the rest of the paper, the high density of useful background galaxies afforded by deep ACS exposures (~72 arcmin^{-2}) allows us to achieve a robust detection of the weak-lensing signal with only 22 galaxies and to study the mass density profile with unprecedented radial resolution.

The paper is organized as follows. After briefly summarizing the gravitational lensing formalism and notation in § 2, we discuss the sample, data reduction and analysis, and the main observational properties of the lens galaxies in § 3. Section 4 details the shear measurement, with a particular emphasis on the precision correction for instrumental systematic effects and on tests of residual systematics by means of a parallel analysis of blank fields. This section also presents the mean radial shear profile around SLACS strong lenses and high-resolution two-dimensional mass reconstructions. We combine strong and weak gravitational lensing constraints in § 5 to model the radial profile lenses and disentangle the stellar and DM components. We discuss our results in § 6 and give a brief summary in § 7.

Throughout this paper we assume the concordance cosmological background with $H_0 = 100\ h$ km s^{-1} Mpc^{-1}, $\Omega_m = 0.3$, and $\Omega_\Lambda = 0.7$. All magnitudes are expressed in the AB system.

2. BASIC LENSING EQUATIONS

In this section we briefly summarize the necessary background of gravitational lensing and especially the weak-lensing regime that concerns the present analysis. The main purpose of this section is to define notations. We refer the reader to the reviews of Mellier (1999), Bartelmann & Schneider (2001), and Schneider (2006) for more detailed accounts.

The fundamental quantity for gravitational lensing is the lens potential $\psi(\boldsymbol{\theta})$ at angular position $\boldsymbol{\theta}$, which is related to the surface mass density $\Sigma(\boldsymbol{\theta})$ projected onto the lens plane through

$$\psi(\boldsymbol{\theta}) = \frac{4G}{c^2}\frac{D_{\rm ol}D_{\rm ls}}{D_{\rm os}}\int d^2\boldsymbol{\theta}'\,\Sigma(\boldsymbol{\theta}')\ln|\boldsymbol{\theta}-\boldsymbol{\theta}'|, \qquad (1)$$

where $D_{\rm ol}$, $D_{\rm os}$, and $D_{\rm ls}$ are angular distances to the lens, to the source, and between the lens and the source, respectively. The deflection angle $\boldsymbol{\alpha} = \nabla\psi$ relates a point in the source plane $\boldsymbol{\beta}$ to its image(s) in the image plane $\boldsymbol{\theta}$ through the lens equation $\boldsymbol{\beta} = \boldsymbol{\theta} - \boldsymbol{\alpha}(\boldsymbol{\theta})$. The local relation between $\boldsymbol{\beta}$ and $\boldsymbol{\theta}$ is the Jacobian matrix $a_{ij} = \partial\beta_i/\partial\theta_j$,

$$a_{ij} = \delta_{ij} - \psi_{,ij} = \begin{pmatrix} 1-\kappa-\gamma_1 & -\gamma_2 \\ -\gamma_2 & 1-\kappa+\gamma_1 \end{pmatrix}. \qquad (2)$$

The convergence $\kappa(\boldsymbol{\theta}) = \Sigma(\boldsymbol{\theta})/\Sigma_{\rm crit}$ is directly related to the surface mass density via the critical density

$$\Sigma_{\rm crit} = \frac{c^2}{4\pi G}\frac{D_{\rm os}}{D_{\rm ol}D_{\rm ls}} \qquad (3)$$

and satisfies the Poisson equation

$$\Delta\psi = \psi_{,11} + \psi_{,22} = 2\kappa. \qquad (4)$$

The two-component shear is $\gamma = \gamma_1 + i\gamma_2 = \frac{1}{2}(\psi_{,11} - \psi_{,22}) + i\psi_{,12}$ in complex notation. An elliptical object in the image plane is characterized by its complex ellipticity e. In the weak-lensing regime, the source intrinsic ellipticity e_s and e are simply related by $e = e_s + \gamma$.

It is convenient to express the shear in a tangential and a curl term $\gamma = \gamma_t + i\gamma_\times$ such that $\gamma_t = -\mathcal{R}\{\gamma e^{-2i\varphi}\}$ and $\gamma_\times = -\mathcal{I}\{\gamma e^{-2i\varphi}\}$, with φ the polar angle. For a circularly symmetric lens, $\gamma_\times$ vanishes, whereas γ_t at radius r can be written as the difference between the mean convergence within that radius $\overline{\kappa}(<r)$ and the local convergence at the same radius $\kappa(r)$:

$$\gamma_t = \overline{\kappa}(<r) - \kappa(r). \qquad (5)$$

In equations (1)–(5) we can isolate a geometric term that linearly scales the lensing quantities κ, ψ, and γ and only depends on the distance ratio $D_{\rm ls}/D_{\rm os}$. We thus can write $\psi = w(z_l, z_s)\psi_\infty$ (and analogously for κ and γ) with $w(z_l, z_s) = D_{\rm ls}/D_{\rm os}\Theta(z_s - z_l)$, where $\Theta(x)$ is the Heaviside step function. If sources are not confined in a thin plane, we account for the distribution in redshift by defining an ensemble average distance factor $\overline{w}(z_l)$ such that

$$\overline{w}(z_l) = \langle w(z_l, z_s)\rangle_{z_s} = \frac{\int_{z_l}^{\infty} dz_s\, n(z_s)(D_{\rm ls}/D_{\rm os})}{\int_0^\infty dz_s\, n(z_s)}. \qquad (6)$$

3. THE DATA

3.1. *Lens Sample*

In this paper we focus on a subsample of 22 lens early-type galaxies taken from the SLACS Survey (Paper I). The subsample is defined as all the confirmed lenses for which deep, one-orbit long, ACS images through filter F814W were available as of the

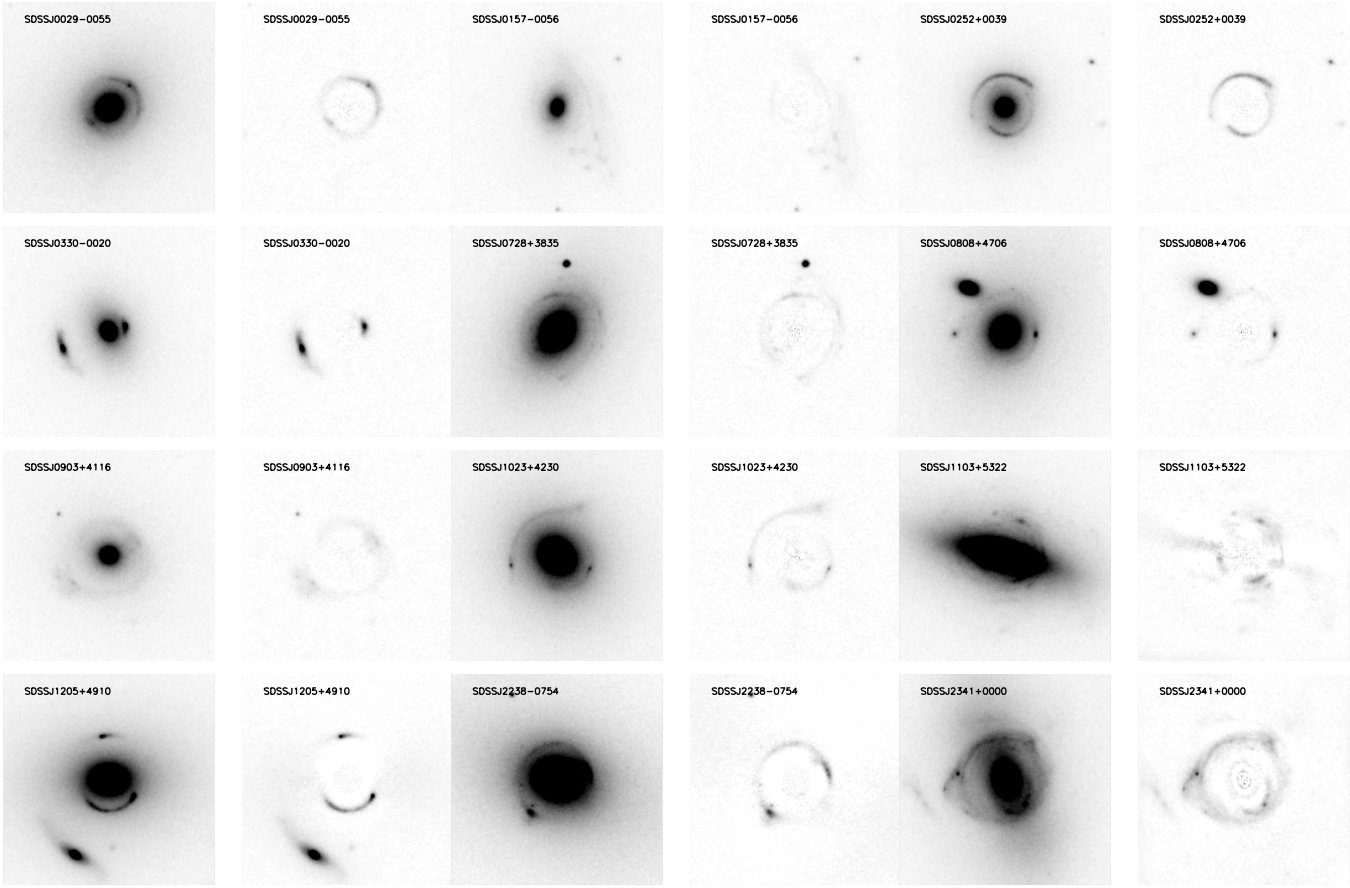

FIG. 1.—F814W gallery of the 12 new SLACS lenses. The postage stamps are 7.2″ on a side. From top to bottom, left to right: SDSS J0029−0055, SDSS J0157−0056, SDSS J0252+0039, SDSS J0330−0020, SDSS J0728+3835, SDSS J0808+4706, SDSS J0903+4116, SDSS J1023+4230, SDSS J1103+5322, SDSS J1205+4910, SDSS J2238−0754, and SDSS J2341+0000. For each lens we show the original image (*left*) and after subtraction of a model for the lens surface brightness (*right*).

cutoff date for this paper, 2006 October 15. The parent sample is spectroscopically identified from the SDSS database and confirmed by ACS imaging, as described in Paper I (see also Bolton et al. 2004). Ten lenses are in common with the sample previously analyzed in Papers II and III, while the remaining 12 lenses were not analyzed in Papers II and III. Images of the 12 new lenses are shown in Figure 1. Table 1 summarizes the most relevant properties of the 22 lenses. More details on the new lenses and on the ongoing programs will be presented elsewhere.

The SDSS aperture velocity dispersions are in the range 196 km $s^{-1} \leq \sigma_v \leq 333$ km s^{-1}, and the mean square velocity dispersion is $\langle \sigma_v^2 \rangle^{1/2} \simeq 248$ km s^{-1}. The lens galaxies have a mean redshift $\langle z_l = 0.22 \rangle$. Paper II showed that SLACS strong lenses fall on the same fundamental plane of nonlens early-type galaxies (see also Bolton et al. 2007). This demonstrates that, within our measurement errors, lensing galaxies have normal internal dynamical properties at small scales. One of the goals of this paper is to combine strong with weak lensing to check whether the outer regions of the SLACS lenses behave in a peculiar way as compared to nonlens early-type galaxies.

3.2. *HST Observations and Data Reduction*

The sample was observed with ACS on board the *Hubble Space Telescope* (*HST*) between 2005 November and 2006 October 15, as part of *HST* programs 10494 (PI: Koopmans) and 10886 (PI: Bolton). One-orbit exposures were obtained through filter F814W (hereafter *I*) with the Wide Field Camera centering the lens on the WFC1 aperture, i.e., in the center of the second CCD. Hence, the observations cover a region as far as 3′ around the lenses. Four subexposures were obtained with a semi-integer pixel offset (ACS-WFC-DITHER-BOX) to ensure proper cosmic-ray removal and sampling of the point-spread function (PSF). For the lenses in program 10494 additional one-orbit exposures with ACS through filter F555W and with the NICMOS NIC2 camera through filter F160W are also available. In this paper, the additional F555W exposure is used to check satellite/foreground contamination to the weak-lensing catalog. A full detailed analysis of the multicolor images will be presented elsewhere.

Since the goal of this paper is detecting the weak-lensing signal produced by the SLACS strong lenses, we optimize our reduction according to the prescriptions of Rhodes et al. (2007, hereafter R07). For each target, we used `multidrizzle` (Koekemoer et al. 2002) to combine the four subexposures, using a final pixel size of 0.03″ and a Gaussian interpolation kernel.

One important difference between this study and that of R07 is that ours are pointed observations. Thus, instrumental effects could play a different role than for weak-lensing studies of objects at random positions on the detector, possibly introducing systematic errors. In order to determine the amplitude of systematic errors in our weak-lensing analysis, we carried out a perfectly analogous analysis of 100 *I* images of COSMOS[7] with identical depth. As detailed below, this allows us to infer the mean and field-to-field variance of instrumental biases, showing that they are negligible for our purposes.

[7] See http://www.astro.caltech.edu/~cosmos/.

TABLE 1
LENS SAMPLE OBSERVED WITH DEEP ACS F814W IMAGING

Name	Program ID	Exposure Time (s)	z_l	σ_{ap} (km s^{-1})	R_{Ein} (arcsec)	R_{eff} (arcsec)	m_I	$M_V + 5\log h$	z_s	w_{SL}	$\overline{w}_{WL}$
SDSS J002907.8−005550	10886	2088	0.227	228 ± 18	0.82	1.48	17.36	−21.53	0.931	0.706	0.721
SDSS J015758.9−005626	10886	2088	0.513	295 ± 47	0.72	0.93	18.76	−22.16	0.924	0.380	0.441
SDSS J021652.5−081345	10494	2232	0.332	333 ± 23	1.15	2.79	16.88	−22.95	0.523	0.333	0.608
SDSS J025245.2+003958	10886	2088	0.280	164 ± 12	0.98	1.69	17.84	−21.67	0.982	0.656	0.662
SDSS J033012.1−002052	10886	2088	0.351	212 ± 21	1.06	1.17	18.20	−21.86	1.107	0.613	0.589
SDSS J072805.0+383526	10886	2116	0.206	214 ± 11	1.25	1.33	16.95	−21.80	0.688	0.660	0.745
SDSS J080858.8+470639	10886	2140	0.219	236 ± 11	1.23	1.65	17.10	−21.77	1.025	0.735	0.730
SDSS J090315.2+411609	10886	2128	0.430	223 ± 27	1.13	1.28	18.19	−22.25	1.065	0.521	0.512
SDSS J091205.3+002901	10494	1668	0.164	326 ± 12	1.61	5.50	15.20	−22.95	0.324	0.472	0.794
SDSS J095944.1+041017	10494	2224	0.126	197 ± 13	1.00	1.99	16.61	−20.94	0.535	0.738	0.840
SDSS J102332.3+423002	10886	2128	0.191	242 ± 15	1.30	1.40	19.93	−21.56	0.696	0.686	0.762
SDSS J110308.2+532228	10886	2156	0.158	196 ± 12	0.84	3.22	16.02	−22.02	0.735	0.749	0.801
SDSS J120540.4+491029	10494	2388	0.215	280 ± 13	1.04	1.92	16.76	−22.00	0.481	0.521	0.735
SDSS J125028.3+052349	10494	2232	0.232	252 ± 14	1.15	1.64	16.78	−22.17	0.795	0.662	0.716
SDSS J140228.1+632133	10494	2520	0.205	267 ± 17	1.39	2.29	16.44	−22.20	0.481	0.543	0.747
SDSS J142015.9+601915	10494	2520	0.063	205 ± 43	1.04	2.49	14.93	−21.04	0.535	0.867	0.919
SDSS J162746.5−005358	10494	2224	0.208	290 ± 14	1.21	2.47	16.79	−22.06	0.524	0.570	0.743
SDSS J163028.2+452036	10494	2388	0.248	276 ± 16	1.81	2.01	16.76	−22.31	0.793	0.639	0.698
SDSS J223840.2−075456	10494	2232	0.137	198 ± 11	1.20	2.33	16.20	−21.58	0.713	0.776	0.827
SDSS J230053.2+002238	10494	2224	0.228	279 ± 17	1.25	2.22	16.91	−22.06	0.463	0.476	0.719
SDSS J230321.7+142218	10494	2240	0.155	255 ± 16	1.64	3.73	15.97	−22.40	0.517	0.670	0.805
SDSS J234111.6+000019	10886	2088	0.186	207 ± 13	1.28	3.20	16.30	−22.14	0.807	0.729	0.768

NOTES.—Apparent I-band magnitudes are not corrected for Galactic extinction. Absolute magnitudes are K-corrected, extinction corrected, and corrected to the sample mean redshift $z = 0.2$ for luminosity evolution using $\log L_V(z = 0.2) = \log L_V(z) + 0.40,\ (z - 0.2)$. Combining measurement errors and uncertainties in various photometric corrections yields a typical error in apparent (absolute) magnitudes ±0.02 (±0.04) mag. Relative uncertainties in R_{Ein} are about 5% and ∼10% for R_{eff}. Since systems are elliptical, both R_{Ein} and R_{eff} are expressed relative to the geometric mean intermediate radius. Parameter w_{SL} is the lensing distance ratio for the strong-lensing event source redshift, whereas $\overline{w}_{WL}$ is the same distance ratio averaged over the redshift distribution of background sources used for weak lensing.

3.3. *Surface Photometry and Lens Models*

Surface photometry of the lens galaxies was obtained by fitting de Vaucouleurs profiles after carefully masking the lensed structures (rings) and any neighboring bright satellites. The two-dimensional parametric fit was carried out using GALFIT (Peng et al. 2002). We checked that our results are consistent with those of Paper II for the 10 lenses previously observed with shallower *HST* snapshot imaging (see corrected Table 2 of Paper II in Treu et al. 2006b).

We determined absolute V-band magnitudes of the lenses taking into account filter transformations and Galactic extinction according to the Schlegel et al. (1998) dust maps. Furthermore, in order to homogenize the sample, we passively evolved all V-band magnitudes to a fiducial redshift $z = 0.2$, using the relation (Treu et al. 2001; Paper II)

$$\frac{d\log(M_*/L_V)}{dz} \simeq -0.40 \pm 0.05, \qquad (7)$$

which is well suited for the massive early-type galaxies we are considering here. We note that the correction is of order a few hundredths dex, and adopting a different passive evolution would not alter our results in any significant way. Thus, the V-band luminosities listed in Table 1 are $z = 0.2$ V-band luminosities and can be considered as fair proxies for the lens stellar mass up to an average stellar mass-to-light ratio $\Upsilon_V \equiv M_*/L_V$.

We measured Einstein radii in full analogy to Paper III; that is, we parameterized the lens potential with a singular isothermal ellipse profile and reconstructed the unlensed source surface brightness nonparametrically to match the observed Einstein ring features. Typical uncertainties on the recovered values of R_{Ein} are ∼0.05 with small variation between lenses. Again, we checked that the present modeling provides consistent results with respect to those in Paper III. A more detailed description of strong-lensing modeling of the 12 new lenses will be given in forthcoming papers.

4. SHEAR ANALYSIS

4.1. *Background Source Selection*

The detection of background sources was done with IMCAT[8] and cross-correlated with the SExtractor (Bertin & Arnouts 1996) source catalog to remove spurious detections. To limit screening by the foreground main lens, we subtracted its surface brightness profile before source detection with SExtractor and IMCAT. After identifying stars in the magnitude-size diagram in a standard manner, we applied the following cuts to select objects for which shapes could be reliably measured. First, we restricted the analysis to galaxies brighter than $I < 26$ although the galaxy sample is complete down to $I \sim 27.5$, based on the number counts. This removes faint and small objects with poorly known redshift distribution. Second, we applied a bright $I \geq 20$ cut to the source sample, to minimize foreground contamination. Third, we discarded objects with a half-light radius $r_h \leq 0.09''$ (for comparison the I PSF has $r_h \sim 0.06''$). Fourth, pairs of galaxies with small angular separation ($\leq 0.5''$) were discarded since their shape cannot be reliably measured. After these cuts, we achieve a number density of useful background sources $n_{bg} = 72$ arcmin^{-2}.

The redshift distribution of sources is taken from the recently published COSMOS sample of faint galaxies detected in the ACS F814W band (Leauthaud et al. 2007). Their analysis exploits photometric redshifts, to derive redshift source distribution down to magnitude $I \simeq 26$ for a sizeable sample selected at *HST* resolution.

[8] See http://www.ifa.hawaii.edu/~kaiser/imcat/.

The redshift distribution of sources having $I \leq 26$ is well represented by the following expression:

$$\frac{dn(z_s)}{dz_s} = \frac{1}{z_0\Gamma(a)} e^{-z_s/z_0} (z_s/z_0)^{a-1}, \quad (8)$$

with $z_0 = 0.345$ and $a = 3.89$. For this particular redshift distribution, values of $\overline{w}_{\rm WL} = \langle D_{\rm ls}/D_{\rm os} \rangle_{z_s}$ are reported in Table 1. This redshift distribution represents a clear improvement of our analysis over previous estimates based on ground-based surveys, as the redshift distribution of faint sources depends not only on magnitude but also on object size. The relatively low redshifts of SLACS lenses and the rapid saturation of $w(z_l, z_s)$ with increasing source redshift help reduce the sensitivity of our results to residual errors on photometric redshifts. Taking into account current errors on $dn(z_s)/dz_s$ reported by Leauthaud et al. (2007), the overall calibration for our sample is accurate to $\sim$7%. In the rest of the paper we show that this uncertainty is negligible for our purposes.

A potential additional concern is residual contamination by satellite galaxies that are spatially correlated with the main lens galaxy and thus could dilute the weak-lensing signal. Furthermore, we expect the number of satellites to depend on the distance from the lens center, and this could potentially affect our inferred shear profile.

As a first check, we applied a color cut to the background catalog of the 10 SLACS fields for which F555W filter imaging is available. We measured the shear signal for galaxies redder than the lenses (i.e., F555W $-$ F814W ≥ 1.5), expected to be at higher redshift (for similar color selections see, e.g., Broadhurst et al. 2005; Limousin et al. 2006). The signal-to-noise ratio (S/N) on the recovered shear profile for this tiny subsample of sources turned out to be too small for this test to be conclusive. This test will be more powerful when the full multicolor data set is available at the end of the survey.

Therefore, we turned to comparisons with the weak-lensing SDSS analysis of S04, who found that about 10% of $r < 22$ sources are correlated to the lens at scales $\sim$30 kpc. Our ACS catalogs are 4 mag deeper than SDSS catalogs. The number density of background sources is much higher, $N_{\rm bg}(I < 26)/N_{\rm bg}(I < 22) \sim 46$, but the number of satellites should also increase. Assuming a typical luminosity function with slope $\alpha = -1$, we can extrapolate our counts and predict that $N_{\rm sat}(I < 26)/N_{\rm sat}(I < 22) \lesssim 2$. Therefore, at $\sim$30 kpc from the lens center, the contamination must be at most $N_{\rm sat}/N_{\rm bg} \simeq 10 \times 2/46 \sim 0.5\%$. Similarly, at smaller scale $r \sim 3$ kpc, we can extrapolate S04 results to predict that the contamination ratio increases by at most a factor of 10, yielding $N_{\rm sat}/N_{\rm bg} \simeq 5\%$. This ratio, as we see below, is much smaller than present error bars ($\gtrsim$30% per bin) so we conclude that contamination by satellites cannot be a significant source of error. This finding is supported by the excellent agreement between strong- and weak-lensing measurements at small scales (see below).

4.2. *Instrumental Distortions*

Before using the shape of background galaxies as a tracer of the shear field, we need to correct several instrumental effects. Because every lens galaxy is approximately[9] at the same location in the detector frame (in the middle of CCD2), we need to carefully assess and correct any instrumental source of systematic polarization of galaxies that may bias the measured shear profile. To correct for the smearing of galaxy shape by the PSF, we use the well-known KSB method (Kaiser et al. 1995), which has proved to be a reliable method down to cosmic shear requirements (Heymans et al. 2006a). The implementation we are using is similar to that of Gavazzi & Soucail (2007) but is tuned for the specific space-based conditions (see, e.g., Hoekstra et al. 1998) by adaptively matching the radial size of the weight function applied to stars to that of the galaxies that are being PSF corrected. Some important changes inspired by R07 are detailed in the following (for further discussion of the techniques required to extract weak-lensing signal from ACS images see also Schrabback et al. 2007).

[9] Typically within a few pixels due to absolute pointing uncertainties. The stack is of course aligned on the measured center of each galaxy.

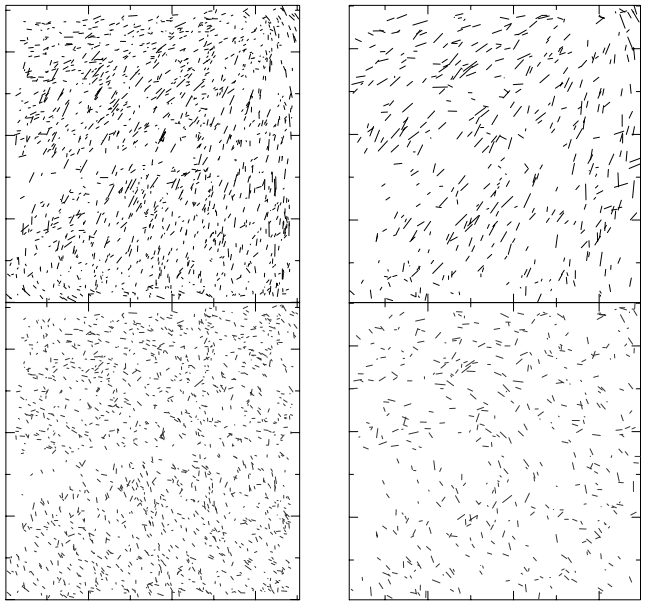

FIG. 2.—Ellipticity patterns measured onto stars in *all* the COSMOS (*left*) and SLACS (*right*) fields. Top panels show stellar ellipticities before applying a PSF correction scheme, whereas the bottom panels show that the main distortion patterns are significantly suppressed after correction. Each panel corresponds to the full ACS field of view (i.e., 200″ on a side). [*See the electronic edition of the Journal for a color version of this figure.*]

4.2.1. *Focus and Point-Spread Function Smearing*

The shape of galaxies must be corrected for the smearing by the PSF of the ACS camera, which circularizes objects and/or imprints systematic distortion patterns. The PSF from space-based images is expected to be more stable as compared to ground-based data, which suffer from time-varying atmospheric seeing conditions. However, R07 showed that the ACS PSF varies dramatically as a function of time, essentially because of focus oscillations due to thermal breathing. The peculiar off-axis position of ACS enhances any focus variability, and PSF anisotropy is difficult to control. Unfortunately, we cannot map PSF variations across the field from the data themselves, since not enough stars are observed in each exposure. Therefore, following R07, we compare the few available stars to mock PSFs built with Tiny Tim (Krist & Hook 2004) and modified as described in R07 as a function of focus and determine the best-fitting focus. The distribution of offsets $\delta_{\rm focus}$ with respect to the nominal ACS focal plane is well consistent with R07, i.e., $\delta_{\rm focus} \sim -3.4 \pm 0.8$ μm. As a consistency check, we apply the same procedure to the blank fields from COSMOS.

Figure 2 shows the ellipticity of stars before and after our PSF correction scheme for the 100 COSMOS fields and our 22 SLACS fields. Averaged over the COSMOS fields we measured

a mean complex ellipticity $\langle e_{*,\rm uncor}\rangle = (-0.0037 + 0.0072i) \pm 0.0004$ before PSF anisotropy correction and $\langle e_{*,\rm cor}\rangle = (0.0000 - 0.0043i) \pm 0.0003$ after correction. Similarly, in SLACS fields we obtained $\langle e_{*,\rm uncor}\rangle = (-0.0025 + 0.0096i) \pm 0.0006$ and $\langle e_{*,\rm cor}\rangle = (0.0011 - 0.0023i) \pm 0.0005$. In both data sets the scatter of corrected stellar ellipticities about this mean is isotropic and $\sigma_{e_{*,\rm cor}} \simeq 0.0087$. We conclude that the correction reduces the *mean* PSF anisotropy by a factor of 2–4 although some residuals are still present at the $\sim$0.003 level. We show in § 4.2.3 that the residual uncertainties are negligible for our purpose.

In addition to anisotropic distortions, the convolution with the PSF also produces isotropic smearing, making objects appear rounder. This effect is much smaller on *HST* images than from the ground, but it must be taken into account for small objects with a typical size comparable to that of the PSF. Our initial size cut $r_h \geq 0.09''$ guarantees that such isotropic smearing is kept at a low level and the KSB method can perform an accurate correction (Kaiser et al. 1995; Hoekstra et al. 1998). Our implementation of KSB builds on the proposed improvements suggested by the STEP1 and STEP2 results (Heymans et al. 2006a; Massey et al. 2007). These papers indicate that, in general, KSB methods can achieve $\sim$10% relative shear calibration biases or smaller. Since this is smaller than our statistical errors, it is sufficient to adopt for the present paper a conservative 10% systematic uncertainty in our shear calibration (*m* STEP parameter). In a future paper we plan to take advantage of the future spaceSTEP simulation set to get a more accurate estimate of the uncertainty on the shear calibration. This will be necessary given the gain in sensitivity expected when the deep SLACS follow-up will be complete. In addition, we demonstrate in the next section that no significant residual additive term (*c* STEP parameter) is observed in either the SLACS data or the COSMOS control fields.

4.2.2. *Charge Transfer Efficiency*

Another source of systematic distortion is the degradation of charge transfer efficiency (CTE) on ACS CCDs. Charges are delayed by defects in the readout direction (i.e., the *y*-axis, charges going from the gap between the CCD chips toward the field boundaries), imprinting a tail of electrons behind each object that modifies its shape, thus producing a spurious negative e_1 component. Since the strength of CTE-induced distortions depends on the S/N of the objects (the fainter the source, the stronger the effect), we cannot measure distortions from stars and correct faint galaxies accordingly. This effect must be quantified and corrected with galaxies themselves, but one must be able to distinguish between the physical signal and the CTE distortions. To this aim we use the blank COSMOS fields to make sure that our CTE correction scheme will efficiently remove CTE distortions while leaving the actual shear signal unchanged. In practice, we use the empirical recipe proposed by R07 in which an $e_{1,\rm CTE}$ component, function of *y* pixel coordinate, S/N, and observation time (since CCD degradation increases with time) are subtracted for each object. Here we adapt the expression from equation (10) of R07,

$$e_{1,\rm CTE} = -3.6\times10^{-4}\left(\frac{1}{2} - \left|\frac{1}{2} - y'\right|\right)\left(\mathrm{S/N}^{-0.9}\right) \times (\mathrm{MJD} - 52{,}333)\left(\frac{r_h}{0.18''}\right)^{-0.1}, \quad (9)$$

to the IMCAT definition of S/N, whereas R07 use SExtractor. Note that the small dependence of $e_{1,\rm CTE}$ on size is somewhat degenerate with the way S/N is defined and may not be always necessary (like in R07). Note also that S/N is calculated by IMCAT without taking into account noise correlation caused by multidrizzling on oversampled pixels ($0.03''$ pixel size instead of the native $0.05''$ value). Therefore, this expression may not be directly applicable with different `multidrizzle` settings. MJD is the Modified Julian Date of observation, r_h is the half-light radius, and y' is the normalized *y* pixel coordinate.[10]

Figure 3 illustrates the effect of CTE on e_1 ellipticity components for COSMOS and SLACS fields (*left and right panels, respectively*). We show the e_1 component of galaxy ellipticity as a function of the y' frame coordinate for sources brighter than $I = 27$ (i.e., well beyond our magnitude cut for selecting suitable sources). The top panels show the mean e_1 before and after CTE(+PSF) correction. For COSMOS and SLACS we see a similar tendency for vertical stretching of galaxies in the middle of the frame. The empirical CTE distortion fitting formula given by equation (9) provides a good correction. Although statistical errors are larger in the SLACS images (5 times smaller sample), we see a modulation of the corrected e_1 component as a function of y' that is not observed in the corrected COSMOS images. As seen below, this is the signature of the signal we are interested in and it should not be erased by the CTE correction scheme [in order to compare this residual with the expected shear, we overlay the $\langle e_1(y')\rangle$ shear signal from an isothermal sphere with Einstein radius $R_{\rm Ein} = 1.2''$]. The bottom panels show how CTE distortions depend on S/N. We have split the galaxy sample into three magnitude quantiles, the bright objects being less distorted. This is well accounted for by the S/N (and size) dependence in equation (9). The overall amplitude of CTE distortion is approximately double for SLACS images because of increasing CCD degradation with time. This is also well captured by equation (9). The median observation date of the 100 COSMOS exposures we are considering is $\overline{\rm MJD}_{\rm cosmos} = 53{,}141$, and for SLACS it is $\overline{\rm MJD}_{\rm slacs} = 53{,}972$.

4.2.3. *Checks on Residuals*

To test the quality of the instrumental systematics correction, we plot in Figure 4 the radial profile of both the tangential e_t and curl $e_\times$ components of the complex ellipticity in COSMOS and SLACS fields (*left and right panels, respectively*). The center is set on the lens for SLACS images and at the same location in the detector frame in COSMOS. If we first focus on the latter images, we see no statistically significant residual e_t or $e_\times$ component, thus showing that we are free from PSF (seen in stars and galaxies) or CTE (seen in galaxies only) systematics. Around SLACS lenses as well, stars do not carry any significant residual e_t or $e_\times$ signal. Therefore, we can safely assume that our systematics correction scheme is accurate enough for the present analysis.[11] Galaxies in SLACS fields clearly carry a strong e_t signal (note the first data point well outside the plotting window), whereas no statistically significant $e_\times$ component is observed as expected for a gravitational lensing origin of this shear signal.

4.3. *Other Sources of Error*

A final additional potential source of systematic uncertainty is the effect of the lens galaxy surface brightness on the ellipticity of background sources at small projected radii. To estimate this effect, we detected and measured object shapes before and after subtraction of the lens surface brightness profile using GALFIT and B-spline techniques developed for the strong-lensing analysis

[10] At the bottom (top) edge of the ACS field of view $y' = 0$ (1).

[11] At the end of the SLACS deep survey, we expect $\sim$80–100 lenses. Since systematics is already below statistical errors in COSMOS (100 fields), our treatment is satisfactory for the final sample.

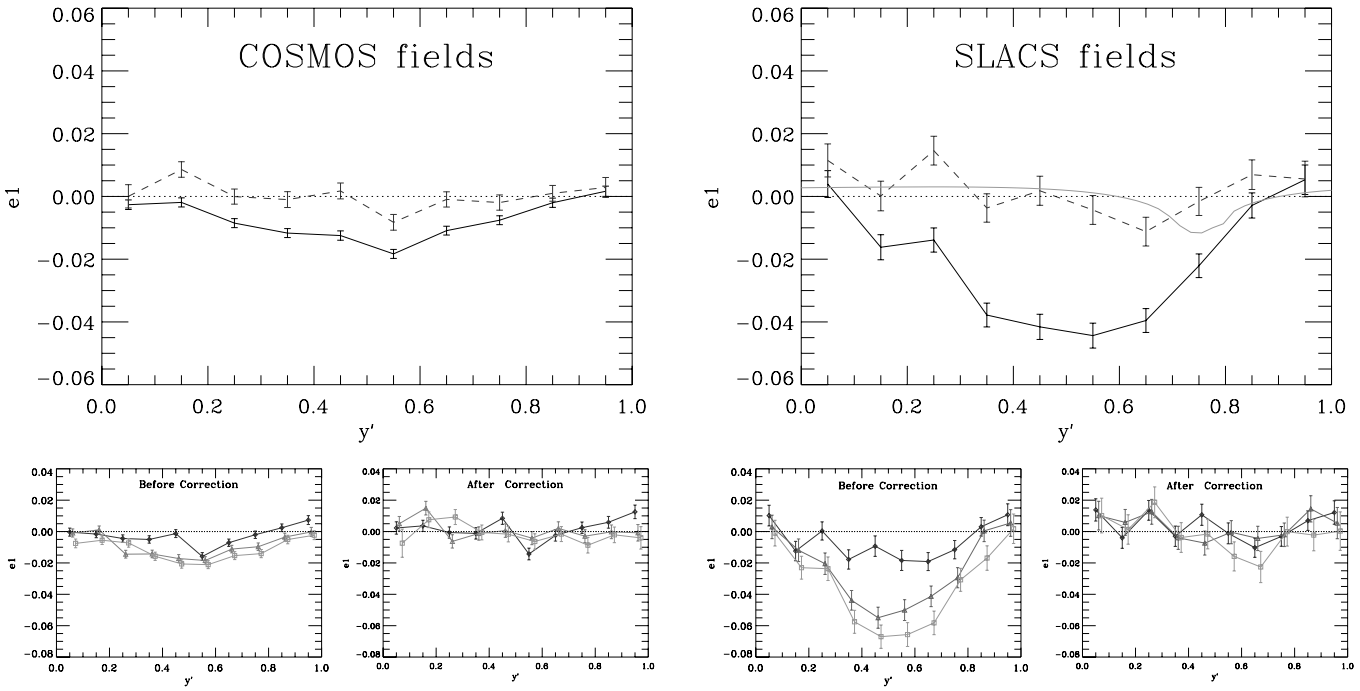

FIG. 3.—Vertical spurious stretching (negative e_1 ellipticity component) as a function of vertical pixel coordinate due to CTE degradation. Measurements for COSMOS and SLACS fields are shown in the left and right panels, respectively. *Top panels*: Average stretching before (*solid line*) and after (*dashed line*) applying our empirical correction term. Distortions are maximum far from the readout (gap between CCDs at $y' \sim 0.5$). They are stronger in SLACS images because the number of defects in CCDs increases with time. The corrected residual signal should not be perfectly "flat" in SLACS fields because of the presence of the true weak-lensing signal we aim at detecting. The amplitude of the mean e_1 shear signal expected from an isothermal sphere with Einstein radius $R_{\rm Ein} = 1.2''$ is shown for comparison (*gray solid line*). The bottom panels show that distortions are stronger for fainter objects as illustrated by splitting galaxies into three magnitude bins. Comparing e_1 ellipticities before (*left*) and after (*right*) applying our correction scheme, we see that eq. (9) corrects this spurious signal at all magnitudes. [*See the electronic edition of the Journal for a color version of this figure.*]

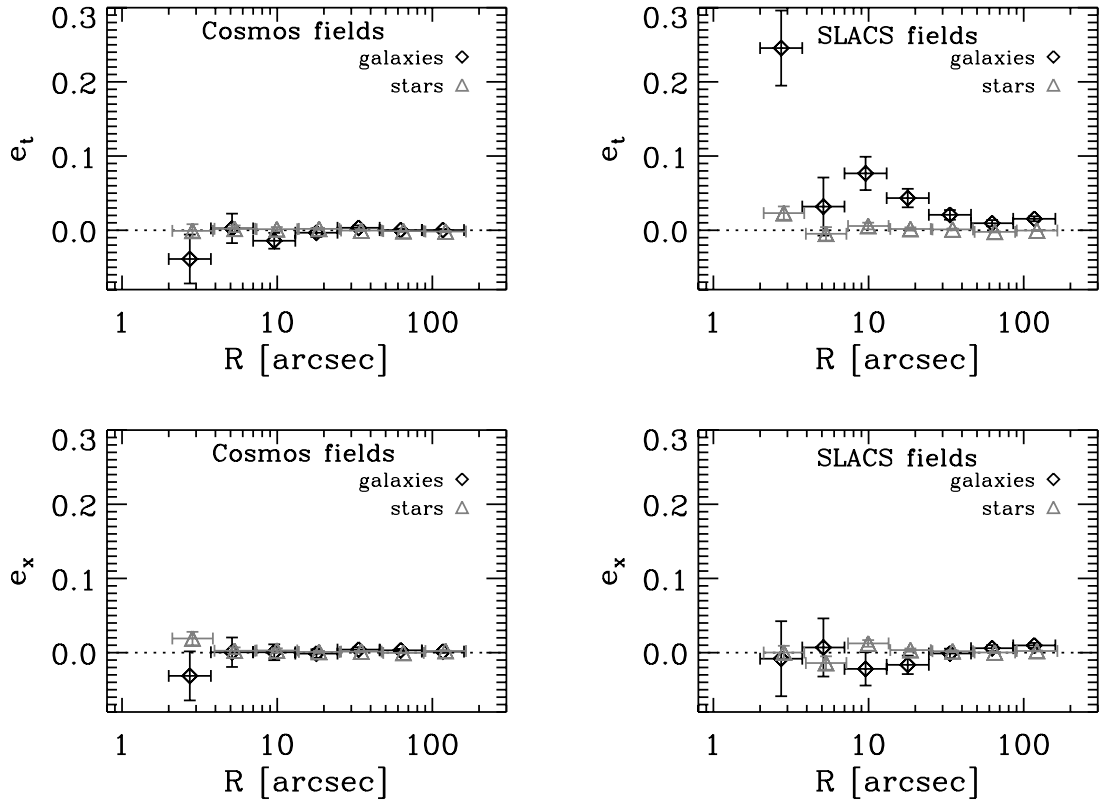

FIG. 4.—Radial ellipticity profile in COSMOS (*left*) and SLACS (*right*) fields. Top panels show the tangential component e_t profile, and bottom panels show the curl component $e_\times$. The signal is measured on both distortion-corrected stars (*triangles*) and galaxies (*squares*). For plotting convenience the innermost data point in the top right panel (e_t in SLACS) falls outside the window. [*See the electronic edition of the Journal for a color version of this figure.*]

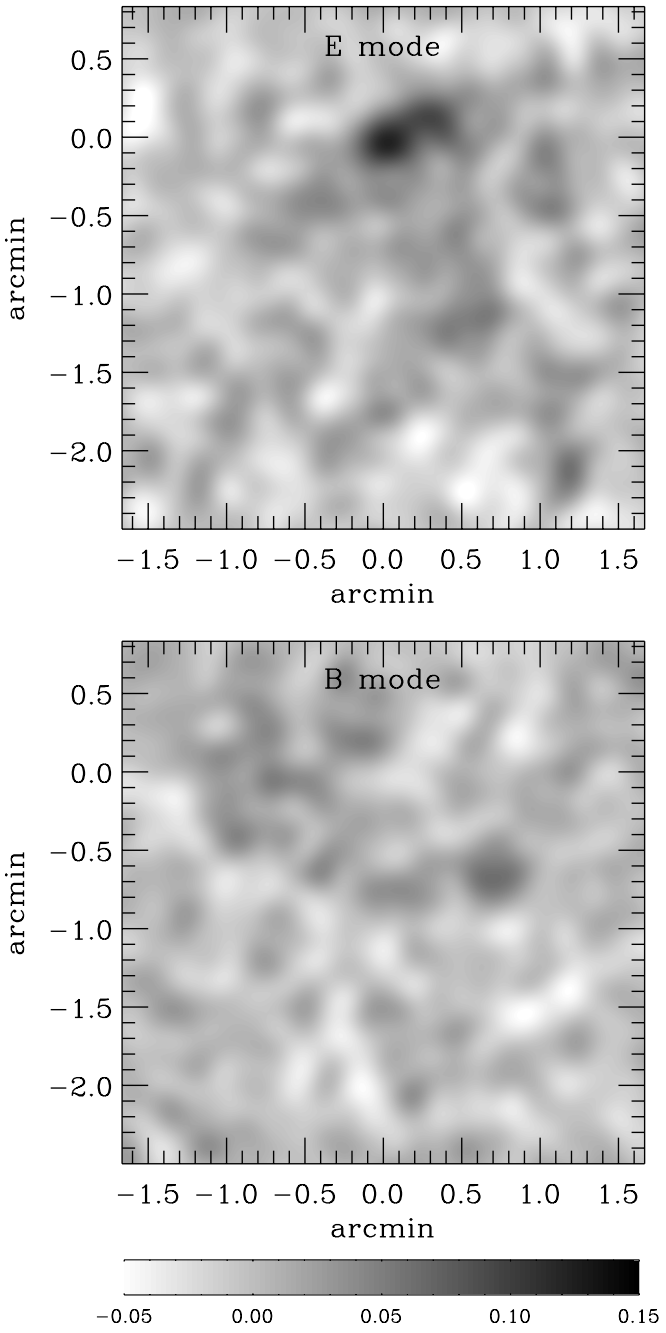

FIG. 5.—Mass reconstruction around stacked SLACS lenses in the same detector frame. The top panel shows the convergence map (E mode), whereas the bottom panel shows the recovered convergence map after rotating galaxies by 45° (B mode), which is consistent with a pure noise realization.

(Paper I). These two methods yield similar results for the purpose of weak lensing. It turns out that the lens subtraction process changes measured ellipticities by at most 5% in an incoherent way. Therefore, we do not consider further the effect of lens surface brightness as a relevant potential source of systematics.

4.4. *Two-dimensional Mass Reconstruction and Shear Profile*

In the top panel of Figure 5 a mass reconstruction (convergence κ map) around the stacked lenses using the Kaiser & Squires (1993) method is shown. There is only one significant convergence peak at the position of the main lens. Note that the Gaussian smoothing scale of the convergence maps is $8''$. This extraordinarily high spatial resolution is made possible by the high density of background sources. The bottom panel shows the imaginary part of the reconstructed mass map (obtained after rotating background galaxies by 45°). This is consistent with a pure noise map and illustrates the amplitude of the noise.

We now analyze the radial shear profile achieved by stacking the lens galaxies. Since the images are taken at a random orientation with respect to the lens major axis, we can safely assume circular symmetry in the analysis. We convert the shear γ into the physical quantity $\Delta\Sigma(R) = \Sigma_{\rm crit}\gamma(R) = \overline{\Sigma}(<R) - \Sigma(R)$. For a given lens redshift z_l we also define the average critical density $\Sigma'_{\rm crit} = (c^2/4\pi G)[1/D_{\rm ol}\overline{w}(z_l)]$. An estimator for $\Delta\Sigma$ at a given radius is

$$\Delta\Sigma = \frac{\sum_{j=1}^{N_{\rm lens}} \Sigma'^{-1}_{{\rm crit}\,j} \sum_{i=1}^{N_{s,j}} e_{t,i}\sigma^{-2}_{e,i}}{\sum_{j=1}^{N_{\rm lens}} \Sigma'^{-2}_{{\rm crit}\,j} \sum_{i=1}^{N_{s,j}} \sigma^{-2}_{e,i}}, \qquad (10)$$

where $N_{s,j}$ is the number of sources in the radial bin around lens j and $\sigma_{e,i}$ is the uncertainty assigned to the tangential ellipticity estimate $e_{t,i}$ (for details on this weighting scheme see Gavazzi & Soucail 2007). With this definition, $\Delta\Sigma$ is directly comparable to other SDSS weak galaxy-galaxy lensing analyses (e.g., S04; M06).

Measured $\Delta\Sigma$ values around SLACS lenses are reported in Table 2 and shown in Figure 6. The detection significance is derived as follows. The χ^2 of the data with respect to the zero shear hypothesis is 47.8 for 9 degrees of freedom. The probability of finding a higher χ^2 is 3×10^{-7}; thus, the nondetection hypothesis is rejected at the 99.99997% level. For a Gaussian distribution this is equivalent to 5 σ.

To compare with previous studies, we consider the measurement from S04 for their subsample of massive $\sigma_v > 186$ km s^{-1}. The mean square velocity of their sample is $\langle\sigma_v^2\rangle^{1/2} \simeq 225$ km s^{-1}. In order to compare with our points, we need to correct for the different velocity dispersion. Assuming an isothermal profile, the shear scales as the velocity dispersion squared, so that we need to scale their points up by $(248/225)^2 \sim 1.21$ for a proper comparison. After this correction, the agreement is excellent in the radial range 60 h^{-1} kpc $\lesssim R \lesssim$ 200 h^{-1} kpc of overlap as shown in Figure 6. We also check that our results are in agreement with the $\Delta\Sigma$ profile of the sm7 (early type) stellar mass bin of M06.

5. JOINT STRONG- AND WEAK-LENSING MODELING

In this section we take advantage of the availability of both strong- and weak-lensing constraints to investigate the mass profile of SLACS lenses from a fraction of the effective radius to 100 effective radii (3 h^{-1} kpc $\lesssim R \lesssim$ 300 h^{-1} kpc).

5.1. *SIS Consistency Check*

Before considering more sophisticated models for the density profile, we first check if the singular isothermal density profile favored in the inner parts of galaxies by strong lensing alone (e.g., Rusin et al. 2003) and by strong lensing and stellar dynamics (Treu & Koopmans 2004; Paper III) is consistent with our weak-lensing measurements.

5.1.1. *Consistency with Strong Lensing*

For a singular isothermal sphere (SIS) the convergence profile as a function of radius R is

$$\kappa(R) = \frac{R_{\rm Ein}}{2R} = \gamma(R), \qquad (11)$$

TABLE 2
Measured Excess Surface Density $\Delta\Sigma$ and Shear γ

Projected Radius (h^{-1} kpc)	$\Delta\Sigma$ ($h\ M_\odot\ \mathrm{pc}^{-2}$)	$\Delta\Sigma_\times$ ($h\ M_\odot\ \mathrm{pc}^{-2}$)	$\sigma_{\Delta\Sigma}$ ($h\ M_\odot\ \mathrm{pc}^{-2}$	γ_t	$\gamma_\times$	σ_γ
3.3.....	2307	−1015	1570	0.339	−0.054	0.093
5.8.....	918	−526	614	0.206	−0.095	0.078
10.1.....	115	141	264	0.074	0.010	0.047
17.6.....	81	−180	153	0.028	−0.011	0.029
30.8.....	232	−36	80	0.064	−0.005	0.017
53.9.....	100	36	46	0.019	0.001	0.010
94.1.....	90	−45	27	0.016	−0.010	0.006
164.5.....	52	52	17	0.010	0.014	0.005
287.5.....	60	34	17	0.014	0.008	0.004

with $R_{\mathrm{Ein}} = 4\pi(\sigma_{\mathrm{SIS}}/c)^2 D_{\mathrm{ls}}/D_{\mathrm{os}}$ in radians and σ_{SIS} the lensing-inferred velocity dispersion, which turns out to be very close to the stellar velocity dispersion σ_* of the lens galaxy (Paper II). For a proper comparison, weak- and strong-lensing measurements have to be renormalized to the same source plane. Hence, the Einstein radius given by strong lens modeling has to be rescaled by a factor $\overline{w}_{\mathrm{WL}}/w_{\mathrm{SL}}$ (see Table 1). Figure 6 shows that after this scaling, but *without fitting any free parameter*, the strong-lensing SIS models provide a reasonably good description of SLACS weak-lensing data out to $\sim$100 h^{-1} kpc (with $\chi^2/\mathrm{dof} \simeq 22.8/9 \simeq 2.5$) and of the SDSS data beyond that (with $\chi^2/\mathrm{dof} \simeq 27.6/9 \simeq 2.7$). Two models are shown: one that neglects the nonlinear relation between reduced shear and ellipticity (*dashed line*), and one that takes this effect into account, as well as the associated nonlinear dependence on the source redshift distribution (*green line*). The two lines differ by less than the error bars of our measurements, showing that a linear relation between ellipticity and shear is a reasonable approximation given the present statistical errors. This analysis shows that the *total* mass density profile of the SLACS lenses is very close to an isothermal sphere with velocity dispersion equal to the stellar velocity dispersion. Since the luminous component is steeper than isothermal outside the effective radius, this finding implies the presence of an extended DM halo that is in turn shallower than isothermal at similar radii.

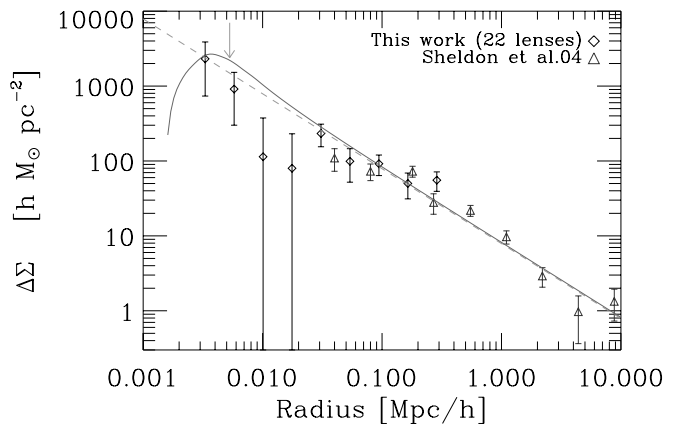

Fig. 6.—Radial shear profile around 22 SLACS strong lenses (*diamonds*) expressed as the excess surface mass density $\Delta\Sigma(R)$. SLACS bins are completely uncorrelated. The gray arrow denotes the mean effective radius of the lenses' stellar component $\overline{R_{\mathrm{eff}}} \simeq 5.3\ h^{-1}$ kpc. The average critical density is $\Sigma_{\mathrm{crit}} \simeq 4620\ h\ M_\odot\ \mathrm{pc}^{-2}$. Previous results from S04 scaled to the same average square velocity dispersion are shown for comparison as triangles (see § 4.4 for details). The lines show the shear profile expected from strong-lensing SIS models. *This is not a fit.* The solid line takes into account nonlinear effects in the relation $\langle e\rangle = g = w\gamma/(1 - w\kappa)$, whereas the dashed line neglects nonlinearities. This shows that $\langle e\rangle = \overline{w}\gamma$ is a good approximation for our purposes. [*See the electronic edition of the Journal for a color version of this figure.*]

5.1.2. *Consistency with Strong Lensing and Stellar Dynamics*

A simple (although model dependent) way to compare on the same plot the mass measurement obtained with strong lensing, stellar dynamics, and weak lensing is obtained in the following manner. For each radial bin we can define an effective weak-lensing velocity dispersion as the velocity dispersion of the SIS that reproduces the shear in that bin. The effective weak-lensing velocity dispersion profile is shown in Figure 7, together with the average stellar velocity dispersion determined from SDSS spectroscopy and the average stellar velocity dispersion of the singular isothermal ellipsoid that best fits the strong-lensing configuration.

The figure illustrates the complementarity of the three mass tracers, stellar velocity dispersion well inside the Einstein radius, strong lensing at the Einstein radius, and weak lensing outside the Einstein radius, as well as the dynamic range of the measurement, almost three decades in radius. The very close correspondence of the stellar and strong-lensing measurement was discussed in Paper II and is confirmed here for a larger sample of lenses. This paper shows that, albeit with larger uncertainties, the weak-lensing data show that the profile is approximately flat for another two decades in radius. This is a qualitative statement as a full joint

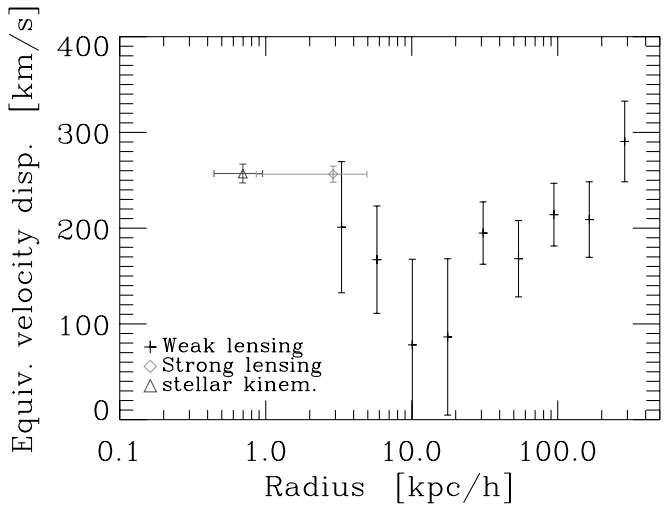

Fig. 7.—Illustration of the complementarity of three mass tracers (stellar velocity dispersion, effective strong- and weak-lensing velocity dispersion) over almost three decades in radius. Stellar velocity dispersion constrains the innermost regions ($\ll R_{\mathrm{Ein}}$), strong lensing the region around the Einstein radius, while weak lensing is most effective beyond the Einstein radius. [*See the electronic edition of the Journal for a color version of this figure.*]

(strong+weak) lensing and dynamical analysis is needed to combine the three diagnostics properly. The three-pronged analysis is beyond the scope of this paper and is left for future work. In the rest of this paper we focus on combining strong and weak lensing in the context of a two-component mass model.

5.2. *Two-Component Models*

In the rest of this section we perform a joint strong- and weak-lensing analysis of the data, in order to disentangle the mass profile of the stellar component and of the surrounding DM halo. For this purpose we adopt a simple two-component model as detailed below. For simplicity, we assume that all lenses are at the center of their halo and none of them are an off-center satellite in a bigger halo. This approximation is well motivated by the galaxy-galaxy lensing results of M06, who found that only a small fraction ($\lesssim$15%) of massive ellipticals do not reside at the center of their host halo. Strictly speaking, the quantity measured by weak lensing is the projected galaxy-mass cross-correlation function rather than the actual shear profile of an individual halo. However, the interpretation of this cross-correlation function within the successful framework of the "halo model" (e.g., Cooray 2006) allows one to disentangle the contribution of the proper halo attached to a given galaxy (one-halo central term), the halo of a more massive host galaxy (or group or cluster) if this galaxy is a satellite (one-halo satellite term), and the contribution due to clustering of neighboring halos about the main halo attached to the galaxy (two-halo term). However, the two-halo terms only provide a significant contribution to the galaxy-mass cross-correlation function beyond a few Mpc (as compared to the outermost $\sim 300\,h^{-1}$ kpc radial bin probed here), and our lenses are massive ellipticals and thus most likely central galaxies. Therefore, for the purpose of this analysis, and given the measured uncertainties, we can assume with little loss of accuracy that the measured shear profile is representative of the only surrounding main halo (see, e.g., Fig. 1 of Mandelbaum et al. 2005).

5.2.1. *Model Definition*

We model the stellar component with a de Vaucouleurs density profile (de Vaucouleurs 1948; Maoz & Rix 1993; Keeton 2001). The effective radius of the stellar component is fixed to the ACS surface photometry. Thus, the only free parameter needed to measure the luminous component is the average stellar mass-to-light ratio Υ_V. The DM halo is assumed to be of the NFW form (Navarro et al. 1997; Bartelmann 1996; Wright & Brainerd 2000), in which the density reads

$$\rho(r) = \rho_c \delta_c \left(\frac{r}{r_s}\right)^{-1} \left(1 + \frac{r}{r_s}\right)^{-2}, \tag{12}$$

with r_s the scale radius and ρ_c the critical density of the universe. The term $\delta_c = (\Delta/3)c^3/[\ln(1+c) - c/(1+c)]$ relates the so-called concentration parameter $c = r_\Delta/r_s$. We assume an overdensity of $\Delta = 119$ so that r_Δ can be considered the "virial" radius (Bryan & Norman 1998). This definition agrees with those of Hoekstra et al. (2005) and Heymans et al. (2006b) for our assumed ΛCDM cosmology. Because statistical errors are still large with only 22 SLACS lenses used here, we lack the sensitivity to constrain the DM profile in detail. Thus, instead of fitting a free concentration parameter, we assume the general relation observed in numerical simulations:

$$c = \frac{9}{1+z}\left(\frac{M_{\rm vir}}{8.12\times10^{12}\ h^{-1}\ M_\odot}\right)^{-0.14} \tag{13}$$

(Bullock et al. 2001; Eke et al. 2001; Hoekstra et al. 2005). In addition, we are not able to constrain the virial mass of each lens individually, so we need to assume a scaling relation between virial mass and V-band luminosity of the form $M_{\rm vir} = \tau_V L_V$. Note that we check that assuming a steeper relation $M_{\rm vir} \propto L_V^{1.5}$ (Guzik & Seljak 2002; Hoekstra et al. 2005; M06) yields comparable results because the SLACS lenses span a narrow range in luminosities, with 0.2 dex rms around $\langle L_V \rangle = 5.70\times10^{10}\ h^{-2}\ L_\odot$. In conclusion, our model has only two free parameters, the mass-to-light ratio of the luminous component Υ_V and the virial mass-to-light ratio τ_V.

Having defined the model, we now define the merit function that will be used to determine the best-fitting parameters with their uncertainties. Detailed strong-lensing analysis of multiply imaged sources has shown that extremely tight constraints can be set on the Einstein radius of individual lenses (e.g., Paper III), with typically a few percent relative accuracy $\sigma_{R_{\rm Ein}}/R_{\rm Ein} \simeq 5\%$. This can be interpreted as a surface mass measurement since the mean density $\overline{\Sigma}$ within this radius is by definition equal to the critical density $\Sigma_{\rm crit}$. Therefore, for each lens we are able to write

$$\overline{\Sigma}(<R_{\rm Ein}) = \Sigma_{\rm crit}(z_l, z_s). \tag{14}$$

The relative error on $R_{\rm Ein}$ translates into $\sigma_{\overline{\Sigma}}/\overline{\Sigma} \simeq 5\%$. We can thus define a strong-lensing merit function:

$$\chi^2_{\rm sl} = \sum_{i=1}^{N_{\rm lens}} \left[\frac{\Sigma_{{\rm crit},i} - \overline{\Sigma}_{*,i}(\Upsilon_V) - \overline{\Sigma}_{{\rm DM},i}(\tau_V)}{\sigma_{\overline{\Sigma}}}\right]^2, \tag{15}$$

where subscripts * and DM stand for luminous and DM components, respectively, evaluated at position $R_{{\rm Ein}_i}$.

In a complete analogy, we define the weak-lensing merit function:

$$\chi^2_{\rm wl} = \sum_{j=1}^{N_{\rm rbin}} \frac{1}{\sigma^2_{\Delta\Sigma,j}} \left\{ \Delta\Sigma_j - \frac{1}{N_{\rm lens}} \sum_{i=1}^{N_{\rm lens}} \left[\Delta\Sigma_{*,ij}(\Upsilon_V) + \Delta\Sigma_{{\rm DM},ij}(\tau_V)\right] \right\}^2, \tag{16}$$

where $N_{\rm rbin}$ is the number of radial bins r_j at which $\Delta\Sigma_j = \Delta\Sigma(r_j)$ is obtained from the weak-lensing data shown in Figure 6.

In the next section we derive the best-fitting $\{\Upsilon_V, \tau_V\}$ values that minimize the total $\chi^2 = \chi^2_{\rm sl} + \chi^2_{\rm wl}$.

5.2.2. *Results*

The top panel of Figure 8 shows the radial profile of the shear for the best-fit model, together with weak-lensing data points. The fit is excellent with a $\chi^2/{\rm dof} = 29.1/31 \simeq 0.94$. We see the detail of the contribution of stellar and DM components. This joint strong+weak-lensing analysis allows us to disentangle the contribution of each. Because the latter component is less concentrated and more extended than the former, there is a radial range $R \sim 20\ h^{-1}$ kpc at which surface mass density flattens. This implies a fast drop in the shear profile $\Delta\Sigma(R)$ at that scale that is quite easy to detect.

In the bottom panel of Figure 8 we show the corresponding three-dimensional mass density profile $\rho(R)$. This profile is close to isothermal although it is made of two components that are not isothermal. The components combine to make an almost isothermal density profile at scales $R \lesssim 100\ h^{-1}$ kpc with a transition from star-dominated to DM-dominated profiles occurring close to the effective radius.

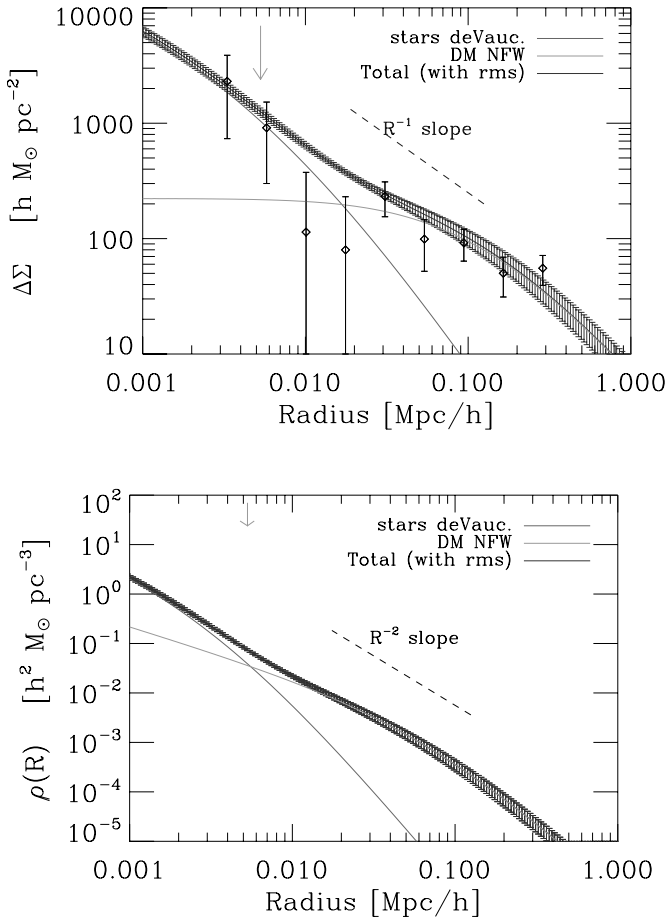

FIG. 8.—*Top*: Shear profile (i.e., $\Delta\Sigma$) for the best DM+de Vaucouleurs profile. The contribution of each mass component is detailed (dark gray and light gray for stars and DM, respectively). The thickness of the black line codes for the 1 σ uncertainty around the total shear profile. Uncertainties are very small below 10 kpc because of strong-lensing data that cannot be shown here. *Bottom*: Similar coding for the three-dimensional density profile $\rho(R)$. The transition between star- and DM-dominated mass profile occurs close to the mean effective radius (*gray arrow*). The total density profile is close to isothermal over roughly two decades in radius. [*See the electronic edition of the Journal for a color version of this figure*.]

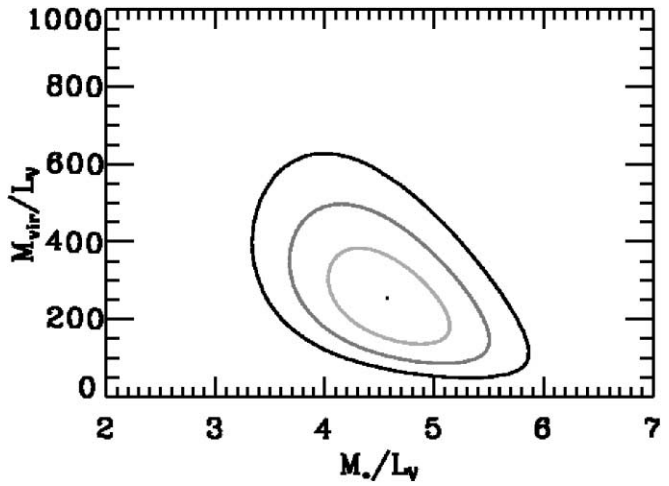

FIG. 9.—Confidence levels around model parameters (1, 2, and 3 σ contours) for the relation between total virial mass-to-light ratio $\tau_V = M_{\rm vir}/L_V$ and stellar mass-to-light ratio $\Upsilon_V = M_*/L_V$. Given the sample mean luminosity $\langle L_V\rangle = 5.7\times10^{10}\ h^{-2}\ L_\odot$, we find a mean sample stellar mass $\langle M_*\rangle = (2.55\pm0.27)\times 10^{11}\ h^{-1}\ M_\odot$ and virial mass $\langle M_{\rm vir}\rangle = 14^{+6}_{-5}\times10^{12}\ h^{-1}\ M_\odot$. [*See the electronic edition of the Journal for a color version of this figure*.]

The best-fit NFW+de Vaucouleurs lens model yields a stellar mass-to-light ratio $\Upsilon_V = 4.48\pm0.46\ h\ M_\odot\ L_\odot^{-1}$ and virial mass-to-light ratio $\tau_V = 246^{+101}_{-87}\ h\ M_\odot\ L_\odot^{-1}$. This translates into a virial-to-stellar mass ratio $M_{\rm vir}/M_* = 54^{+28}_{-21}$. Note that stellar mass-to-light ratio depends in the same way on h as virial mass as they are inferred from lens modeling and not from stellar evolution models. Thus, $M_{\rm vir}/M_*$ is independent of h. Figure 9 shows the 68.3%, 95.4%, and 99.7% confidence level (CL) contours for the best-fit model parameters. A model having a constant mass-to-light ratio (i.e., $M_{\rm vir}/L_V = 0$) is ruled out at $\sim4\ \sigma$.

Given the sample mean luminosity $\langle L_V\rangle = 5.7\times10^{10}\ h^{-2}\ L_\odot$, we find a mean sample stellar mass $\langle M_*\rangle = (2.55\pm0.26)\times 10^{11}\ h^{-1}\ M_\odot$ and virial mass $\langle M_{\rm vir}\rangle = 14^{+6}_{-5}\times10^{12}\ h^{-1}\ M_\odot$. This translates into a mean virial (scale) radius $r_{\rm vir} = 393^{+47}_{-53}\ h^{-1}$ kpc ($r_s = 58\pm8\ h^{-1}$ kpc). We note that the virial radius is typically larger than our field of view, and therefore virial masses rely on extrapolations of our results. Therefore, we also present more robust measurements like the projected and three-dimensional mass within a reference radius $R = 200\ h^{-1}$ kpc. Lens modeling yields $M_{\rm 3D}(<200\ h^{-1}\ {\rm kpc}) = (8.1\pm1.8)\times10^{12}\ h^{-1}\ M_\odot$ and a projected mass $M_{\rm 2D}(<200\ h^{-1}\ {\rm kpc}) = (10.8\pm2.7)\times10^{12}\ h^{-1}\ M_\odot$ (68% CL errors).

To compare with local measurements, we convert our Υ_V mass-to-light ratio to the rest-frame B band. Assuming a typical $(B-V) = 0.96$ color for ellipticals (Fukugita et al. 1995), $(B-V)_\odot = 0.65$, and a Hubble constant $h = 0.7$, one finds $\Upsilon_B = 4.17\pm0.44\ M_\odot\ L_\odot^{-1}$. Using Paper II, Treu & Koopmans (2004), and similar findings (Treu & Koopmans 2002; Treu et al. 2005; van der Wel et al. 2005; di Serego Alighieri et al. 2005) for the passive evolution of massive early-type galaxies, we get a redshift zero B-band stellar mass-to-light ratio $\sim5.81\pm0.61$, which is statistically consistent with local estimates such as $\Upsilon_B = 7.8\pm2.7$ and 7.1 ± 2.8 from Gerhard et al. (2001) and Trujillo et al. (2004), respectively. The low value of M_*/L is also in broad agreement with stellar evolution models of Bruzual & Charlot (2003) although detailed comparisons depend on the assumed initial mass function (IMF).

Our modeling can be used to relate the V-band luminosity within the Einstein radius $\overline{L}_V(<R_{\rm Ein})$ and the fraction of DM in the same projected radius $f_{\rm DM,2D}(<R_{\rm Ein})$. Using equation (14), for a given stellar mass-to-light ratio each lens must verify

$$f_{\rm DM,2D}(<R_{\rm Ein}) = 1 - \Upsilon_V\overline{L}_V(<R_{\rm Ein})/\Sigma_{\rm crit}. \qquad (17)$$

Figure 10 shows the inferred projected $f_{\rm DM,2D}$ using our best-fit $\Upsilon_V = 4.48\ h^{-1}\ M_\odot\ L_\odot^{-1}$. The mean DM fraction within the Einstein radius $\langle f_{\rm DM,2D}\rangle = 0.37\pm0.04$ with 18% rms scatter. Extrapolating to the effective radius, about half of the projected mass is in the form of DM. The result from the NFW+de Vaucouleurs parameterization is shown as the solid line, which matches the data points well (see also Papers II and III). This parameterization also allows the deprojected DM fraction to be calculated and is found to be $\sim$27% (*dotted line*) within $R_{\rm eff}$. The local deprojected DM and stellar densities are of the same order at that radius.

It may seem that the two data points with $f_{\rm DM,2D}\simeq0$ are responsible for our inferred low M_*/L. Since these two lenses have the most elongated stellar component,[12] the assumption of circular symmetry may break down for them. Furthermore, if they

[12] Here $q_* = (b/a)_* \sim 0.5$, whereas the other lenses have a mean $q_* = 0.81$ and dispersion 0.08.

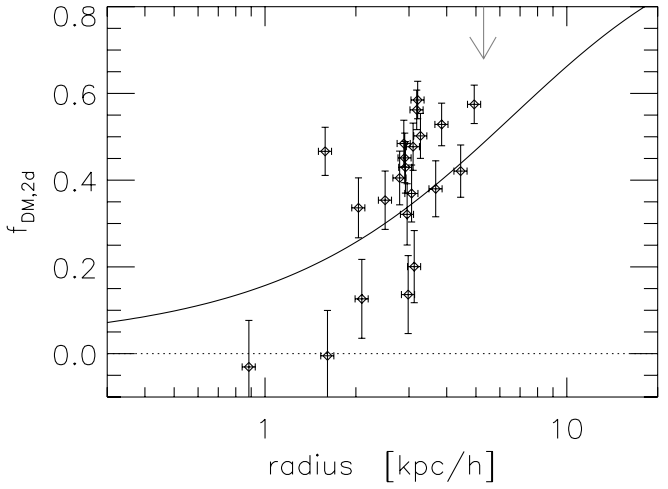

FIG. 10.—Projected DM fraction in SLACS lenses as measured from strong lensing at the Einstein radius (data points) and our constraints on the stellar M_*/L ratio. The Einstein radius is expressed in physical units, and the solid line shows the best-fit profile of the DM fraction $f_{\rm DM,2D}$ inferred from the parametric NFW+de Vaucouleurs modeling of strong+weak-lensing data. The mean effective radius is shown as a gray arrow. We see that $f_{\rm DM,2D}(<R_{\rm eff}) \simeq 50\%$ of the projected enclosed mass is in the form of DM within the effective radius. [*See the electronic edition of the Journal for a color version of this figure.*]

have a disk component with younger stars, this could reduce their global M_*/L with respect to that of pure spheroidal systems. However, redoing the strong+weak-lens modeling without these does not change the stellar mass-to-light ratio too significantly ($M_*/L_V = 4.90 \pm 0.53\ h^{-1}\ M_\odot\ L_\odot^{-1}$).

5.3. *Comparison to Previous Galaxy-Galaxy Lensing Works*

We first compare our findings to the SDSS weak galaxy-galaxy lensing analysis of M06, who defined $M_{\rm cent}$ as the mass enclosed in a sphere within which the mean density is 180 times the background density, similar to our definition. Our lens sample should be compared to the sm7 stellar mass bin for early-type galaxies with $\langle M_*\rangle = 39.6\times10^{10}\ M_\odot$. It would also lie between l6b and l6f early-type galaxy luminosity bins with a typical $\langle L\rangle \simeq 6.3L_*$. To convert the rest-frame V band to the SDSS r' band, we use $V - r' \simeq 0.36$ for ellipticals (Fukugita et al. 1995). Since at the exponential tail of the luminosity and mass functions one is highly sensitive to the scatter in the mass-luminosity relation, M06 applied corrections calibrated into simulations (Mandelbaum et al. 2005), whereas our analysis does not attempt to correct for this effect. For the l6f bin, $M_{\rm cent}/L_r = 674^{+210}_{-203}\ h\ M_\odot\ L_\odot^{-1}$ as found by M06 yields $M_{\rm cent}/L_V = 896 \pm 275\ h\ M_\odot\ L_\odot^{-1}$ (95% CL). Likewise, the sm7 bin of M06 yields $M_{\rm cent}/M_* = 256^{+44}_{-68}$ (95% CL and using $h = 0.7$). These values are significantly larger than our results. However, if we apply a similar correction as these authors, our virial mass should be raised by 66%, yielding $M_{\rm vir}/L_V = 408^{+168}_{-144}\ h\ M_\odot\ L_\odot^{-1}$ and $M_{\rm vir}/M_* = 89^{+46}_{-35}$. The latter correction thus brings our findings into statistical agreement. The small difference might be due to our inability to probe the very outer parts of halos and efficiently constrain virial masses. However, we emphasize that the availability of strong-lensing constraints puts tight constraints on the column density enclosed by $R_{\rm Ein}$, which means that the outer parts of halos cannot contribute much in making lens galaxies critical, or perhaps the fact that we fit for M_*/L while M06 use the value determined from stellar population synthesis models. Issues related to comparisons between Guzik & Seljak (2002) and M06 results are addressed in the latter paper. In any case, we find a much better agreement between our $M_{\rm vir}$ measurement and those of Guzik & Seljak (2002), which give $M_{\rm vir}/L_V \simeq 296 \pm 51\ h\ M_\odot\ L_\odot^{-1}$ after matching our lens sample selection.

We now compare our analysis with the Hoekstra et al. (2005) results. Since we chose to match their definition of virial mass and concentration, we expect comparisons to be easier although the mean redshift of their lens sample is $\sim$0.32. Our lens sample would passively brighten to $\langle L_V\rangle \simeq 6.3\times10^{10}\ h^{-2}\ L_\odot$ at $z = 0.32$, which is $\sim$2.45 times brighter than their higher luminosity bin having $L_V \simeq 2.45\times10^{10}\ h^{-2}\ L_\odot$. Therefore, we need to extrapolate their results using their $M_{\rm vir}\propto L^{1.5}$ relation. They find $M_{\rm vir}/L_V \simeq 253^{+38}_{-35}\ h\ M_\odot\ L_\odot^{-1}$. This value is statistically consistent with ours. However, a detailed comparison is made difficult due to the fact that the authors mix early- and late-type galaxies and they avoid lens galaxies in dense environments. Using stellar evolution models, they estimate the virial-to-stellar mass ratio in their reddest subsample $(B-V)_{\rm rest}\sim 0.95$ to be $M_{\rm vir}/M_* \simeq 43 \pm 6$ for a scaled Salpeter IMF (Bell & de Jong 2001) or $M_{\rm vir}/M_* \simeq 27 \pm 4$ for a PEGASE Salpeter IMF. The scaled Salpeter IMF hypothesis turns out to be in better agreement with our measurements. In addition, it predicts stellar mass-to-light ratios $\Upsilon_B \sim 4.5$ (solar units) closer to our estimates than the PEGASE IMF, which predicts $\Upsilon_B \sim 6.5$.

Finally, Heymans et al. (2006b) measure virial masses of lens galaxies in the range $0.2 \le z_l \le 0.8$ in a narrow range of luminosity $L_r = 2.4\times10^{10}\ h^{-2}\ L_\odot$ with a 0.2 dex dispersion about this mean. This sample is dominated by early-type galaxies. Again, extrapolation to our sample mean luminosity is somewhat uncertain, but, using the $M_{\rm vir}\propto L_V^{1.5}$ scaling, their results give $M_{\rm vir}/M_* = 76 \pm 25$, which is in excellent agreement with our $M_{\rm vir}/M_* = 54^{+28}_{-21}$.

These comparisons show that our virial mass estimates are in good agreement with other studies after extrapolation of our constraints on the radial shear profile (ending around $\sim$300 h^{-1} kpc) out to the virial radius $\sim$480 h^{-1} kpc. Comparing with other results obtained for less massive systems on average increases uncertainties. However, our results on the halo virial masses are well consistent with this ensemble of results above as they lie in between them. In addition, the measured shear profile remarkably matches those of S04 and M06 in the radial range 30 h^{-1} kpc $\lesssim R \lesssim$ 300 h^{-1} kpc. This gives a valuable support to the validity of our results and the control of systematic effects.

6. DISCUSSION

Our joint weak+strong-lensing modeling of SLACS lenses with a two-component mass model allowed us to successfully disentangle the contribution of each, giving sensible results for both the stellar mass-to-light ratio $M_*/L_V = 4.48 \pm 0.46\ h\ M_\odot\ L_\odot^{-1}$ and virial mass-to-light ratio $M_{\rm vir}/L_V = 246^{+101}_{-87}\ h\ M_\odot\ L_\odot^{-1}$, in good agreement with other studies. Assuming NFW and de Vaucouleurs forms for each density profile provides a good description of the data ($\chi^2 \simeq 0.94$ per degree of freedom).

This analysis shows that the total density profile is close to isothermal out to $\sim$100 h^{-1} kpc. It is now well established from SLACS (Paper III) and earlier strong-lensing studies (e.g., Treu & Koopmans 2002, 2004; Rusin et al. 2003; Rusin & Kochanek 2005) that the *total* mass profile of lens galaxies is close to isothermal ($\rho\propto r^{-2}$) within $R_{\rm eff}$. In Paper III this result was established by combining strong lensing and stellar kinematics. The present analysis extends and strengthens this result as we find that the DM and stellar components combine themselves to form an isothermal total density profile well beyond the effective radius.

We find that the transition from a star-dominated to a DM-dominated density profile must occur close to $R_{\rm eff}$. This peculiar transition is also observed by Treu & Koopmans (2004), who

combined strong lensing and stellar kinematics in higher redshift lenses. Similar results can be found in Mamon & Łokas (2005a, 2005b). In addition, the "mean" fraction of DM $f_{\rm DM,3D}(<R_{\rm eff}) \sim 30\%$ is in excellent agreement with local estimates (Kronawitter et al. 2000; Gerhard et al. 2001; Borriello et al. 2003). See also Cappellari et al. (2006) for more recent results from the SAURON project. At this point, it is noteworthy to note an important result of Paper II, that is, strong-lensing galaxies have similar internal properties as normal early-type galaxies in terms of their location in the fundamental plane. Our findings can thus be generalized.

We emphasize that we did not investigate other parameterizations for the DM halo. For instance, a steeper profile ($\rho_{\rm DM} \propto r^{-\alpha}$ with $\alpha > 1$) could possibly arise from the adiabatic contraction (Blumenthal et al. 1986; Gnedin et al. 2004) of an NFW halo that is found in pure DM *N*-body cosmological simulations made without taking into account the complex physics of baryons. With the small sample of lenses we are considering here, we are not sensitive yet to that level of detail in the inner slope of the assumed DM profiles.

We note, however, that the rather low values of M_*/L_V we find would make it unlikely to have a DM halo much steeper than NFW ($\rho \propto r^{-1}$ at the center; see also Borriello et al. 2003; Humphrey et al. 2006). Since it is reasonable to assume that baryons somehow perturb the DM halo within the effective radius, we emphasize that our successful NFW parameterization should rather be considered as a fitting formula for the perturbed halo. In future papers, with the complete observed lens sample and spatially resolved measurements of stellar kinematics, we plan to determine with unprecedented accuracy the inner slope of the DM profile below $R_{\rm eff}$ and at the same time M_*/L_V.

The inner regions of lens galaxies can be considered as representative of the whole parent sample of early-type galaxies as shown in Paper II. Although there is no firm observational evidence, it is thought that environmental effects may bias the population of lens galaxies since extra convergence coming from surrounding large-scale structure may boost lens efficiency while leaving the internal dynamics of lens galaxies unchanged (see also Keeton & Zabludoff 2004; Fassnacht et al. 2006). In the present analysis we address the issue of whether lenses are representative of the overall population at larger radii, by comparing our weak-lensing results with those obtained for nonlens samples. The present analysis shows that, on intermediate scales $R_{\rm eff} < R \lesssim 300\ h^{-1}$ kpc, SLACS massive lenses have the same shear properties as normal ellipticals as found by M06 or S04. We find a good agreement between our virial mass estimates and semi-analytic predictions like those developed in the "halo model" (Mandelbaum et al. 2005; M06; Cooray 2006), as well as with kinematical studies of satellite galaxies (Conroy et al. 2007). Any systematic environmental effect able to perturb shear measurement on those scales is below our present observational uncertainties. When the ACS follow-up is finished, the weak-lensing analysis will provide important new information on the environment of strong lens galaxies. This issue is deferred for a future work.

In terms of the internal structure of early-type galaxies, the present analysis strengthens and extends the results presented in Paper III and gives additional support to the picture proposed there for their formation. The isothermal density profile must be produced at early stages of their evolution process ($z \gtrsim 2$) by merging/accretion involving dissipative gas physics to quickly increase the central phase-space density since pure collisionless systems would rather develop shallower density slopes $\rho \propto r^{[-1,\,-1.5]}$ (e.g., Navarro et al. 1997, 2004; Moore et al. 1998; Ghigna et al. 1998; Jing 2000). Once isothermality is set, early-type galaxies may evolve passively, or they may keep growing quiescently via collisionless "dry" mergers or by accretion of satellites, which preserve the inner density profile of collisionless materials (stars and/or DM). See discussion in Paper III and references therein for further details.

7. SUMMARY AND CONCLUSIONS

We demonstrate that, using deep ACS images, it is possible to measure a weak-lensing signal for a modest sample of massive early-type galaxies [$\sigma_v \sim 250$ km s^{-1} or $\log(M_*/M_\odot) \sim 11.35$]: with only 22 lenses we are able to detect shear signal at 5 σ significance. Key to this success is the large density of well-resolved background sources afforded by ACS, which beats down shot noise and reduces the problem of dilution by lens satellites since background sources greatly outnumber satellites. In addition, these lenses are very distant from one another and hence completely statistically independent. Furthermore, special care has been taken to control systematic errors, using the most advanced techniques to model and correct for the ACS PSF and other instrumental effects. By analyzing a sample of 100 blank fields from COSMOS, we show that residual systematics in the shear measurement is less than 0.3%.

Although weak lensing alone can provide interesting results on lens density profiles at intermediate scale, the great power and originality of this work is the combination of strong- and weak-lensing constraints. Modeling weak *and* strong lensing in massive ($\langle\sigma_v^2\rangle^{1/2} \simeq 248$ km s^{-1}) SLACS galaxies as a sum of stellar (de Vaucouleurs) plus DM halo (NFW) components, we could disentangle the contribution of the two components' overall mass budget. The main results of this joint analysis can be summarized as follows:

1. The total density profile is close to isothermal from $0.5R_{\rm eff} \lesssim R \lesssim 100R_{\rm eff}$ although neither the stellar nor the DM density profile is isothermal.
2. The transition from star-dominated to DM-dominated density occurs at $\sim R_{\rm eff}$, leading to a DM fraction within this radius $f_{\rm DM,3D}(<R_{\rm eff}) = 27\% \pm 4\%$.
3. The best-fit stellar mass-to-light ratio is $M_*/L_V = 4.48 \pm 0.46\ h\ M_\odot\ L_\odot^{-1}$, in agreement with local results and old stellar populations.
4. The best-fit virial mass-to-light ratio is $M_{\rm vir}/L_V = 246^{+101}_{-87}\ h\ M_\odot\ L_\odot^{-1}$, in agreement with galaxy-galaxy weak-lensing results of nonlens galaxies. We found a mean virial mass and radius $\langle M_{\rm vir}\rangle = 14^{+6}_{-5} \times 10^{12}\ h^{-1}\ M_\odot$ and $r_{\rm vir} = 393 \pm 50\ h^{-1}$ kpc, respectively.
5. The agreement with other weak-lensing studies shows that the outer halos of lenses and nonlenses are consistent within the errors. In other words, if lens early-type galaxies live in peculiar environments, their effect on the shear profile down to $300\ h^{-1}$ kpc from the lens center is below our statistical errors.

We forecast a $\sim 10\ \sigma$ detection by the end of the ongoing deep follow-up imaging with *HST* ACS. When completed, the SLACS sample of lenses with well-resolved kinematics will provide valuable constraints on stellar populations and density profiles of both stellar and DM components down to several hundred kiloparsecs of the lens center, thus allowing us to address internal properties of lens galaxies, as well as the effect of their environment. To complete the picture on early-type galaxies and structure formation, it is important to extend SLACS results to higher redshift by increasing the number of such strong lenses through new observational efforts.

We thank Konrad Kuijken and Kevin Bundy for useful suggestions and Phil Marshall for a careful reading of the paper. We would also like to acknowledge insightful discussions with Alexie Leauthaud on the redshift distribution of sources in COSMOS. R. G., T. T., L. V. E. K., A. S. B., and L. A. M. would like to thank the Kavli Institute of Theoretical Physics and its staff for the warm hospitality during the program "Applications of Gravitational Lensing," when a significant part of the work presented here was carried out. The work of L. A. M. was carried out at Jet Propulsion Laboratory, California Institute of Technology under a contract with NASA. This research is supported by NASA through *Hubble Space Telescope* programs SNAP-10174, GO-10494, SNAP-10587, GO-10798, and GO-10886 and in part by the National Science Foundation under grant PHY99-07949. T. T. acknowledges support from the NSF through CAREER award NSF-0642621. Based on observations made with the NASA/ESA *Hubble Space Telescope*, obtained at the Space Telescope Science Institute, which is operated by the Association of Universities for Research in Astronomy, Inc., under NASA contract NAS 5-26555. This project would not have been feasible without the extensive and accurate database provided by the Sloan Digital Sky Survey (SDSS). Funding for the creation and distribution of the SDSS Archive has been provided by the Alfred P. Sloan Foundation, the Participating Institutions, the National Aeronautics and Space Administration, the National Science Foundation, the US Department of Energy, the Japanese Monbukagakusho, and the Max-Planck Society. The SDSS Web site is http://www.sdss.org. The SDSS is managed by the Astrophysical Research Consortium (ARC) for the Participating Institutions. The Participating Institutions are the University of Chicago, Fermilab, the Institute for Advanced Study, the Japan Participation Group, Johns Hopkins University, the Korean Scientist Group, Los Alamos National Laboratory, the Max-Planck-Institute for Astronomy (MPIA), the Max-Planck-Institute for Astrophysics (MPA), New Mexico State University, University of Pittsburgh, University of Portsmouth, Princeton University, the United States Naval Observatory, and the University of Washington.

REFERENCES

Arnaboldi, M., Gerhard, O., Aguerri, J. A. L., Freeman, K. C., Napolitano, N. R., Okamura, S., & Yasuda, N. 2004, ApJ, 614, L33
Bartelmann, M. 1996, A&A, 313, 697
Bartelmann, M., & Schneider, P. 2001, Phys. Rep., 340, 291
Bell, E. F., & de Jong, R. S. 2001, ApJ, 550, 212
Bertin, E., & Arnouts, S. 1996, A&AS, 117, 393
Bertin, G., et al. 1994, A&A, 292, 381
Blumenthal, G. R., Faber, S. M., Flores, R., & Primack, J. R. 1986, ApJ, 301, 27
Bolton, A. S., Burles, S., Koopmans, L. V. E., Treu, T., & Moustakas, L. A. 2006, ApJ, 638, 703 (Paper I)
Bolton, A. S., Burles, S., Schlegel, D. J., Eisenstein, D. J., & Brinkmann, J. 2004, AJ, 127, 1860
Bolton, A. S., Burles, S., Treu, T., Koopmans, L. V. E., & Moustakas, L. A. 2007, ApJ, submitted (astro-ph/0701706)
Borriello, A., Salucci, P., & Danese, L. 2003, MNRAS, 341, 1109
Bradač, M., Schneider, P., Lombardi, M., & Erben, T. 2005a, A&A, 437, 39
Bradač, M., et al. 2005b, A&A, 437, 49
Brainerd, T. G., Blandford, R. D., & Smail, I. 1996, ApJ, 466, 623
Broadhurst, T., Takada, M., Umetsu, K., Kong, X., Arimoto, N., Chiba, M., & Futamase, T. 2005, ApJ, 619, L143
Bruzual, G., & Charlot, S. 2003, MNRAS, 344, 1000
Bryan, G. L., & Norman, M. L. 1998, ApJ, 495, 80
Bullock, J. S., Kolatt, T. S., Sigad, Y., Somerville, R. S., Kravtsov, A. V., Klypin, A. A., Primack, J. R., & Dekel, A. 2001, MNRAS, 321, 559
Cappellari, M., et al. 2006, MNRAS, 366, 1126
Comerford, J. M., Meneghetti, M., Bartelmann, M., & Schirmer, M. 2006, ApJ, 642, 39
Conroy, C., et al. 2007, ApJ, 654, 153
Cooray, A. 2006, MNRAS, 365, 842
de Blok, W. J. G., Bosma, A., & McGaugh, S. 2003, MNRAS, 340, 657
De Lucia, G., Kauffmann, G., Springel, V., White, S. D. M., Lanzoni, B., Stoehr, F., Tormen, G., & Yoshida, N. 2004, MNRAS, 348, 333
de Vaucouleurs, G. 1948, Ann. d'Astrophys., 11, 247
di Serego Alighieri, S., et al. 2005, A&A, 442, 125
Eke, V. R., Navarro, J. F., & Steinmetz, M. 2001, ApJ, 554, 114
Fassnacht, C. D., Gal, R. R., Lubin, L. M., McKean, J. P., Squires, G. K., & Readhead, A. C. S. 2006, ApJ, 642, 30
Fukugita, M., Shimasaku, K., & Ichikawa, T. 1995, PASP, 107, 945
Gao, L., White, S. D. M., Jenkins, A., Stoehr, F., & Springel, V. 2004, MNRAS, 355, 819
Gavazzi, R. 2005, A&A, 443, 793
Gavazzi, R., Fort, B., Mellier, Y., Pelló, R., & Dantel-Fort, M. 2003, A&A, 403, 11
Gavazzi, R., & Soucail, G. 2007, A&A, 462, 459
Geiger, B., & Schneider, P. 1998, MNRAS, 295, 497
Gentile, G., Salucci, P., Klein, U., Vergani, D., & Kalberla, P. 2004, MNRAS, 351, 903
Gerhard, O., Kronawitter, A., Saglia, R. P., & Bender, R. 2001, AJ, 121, 1936
Ghigna, S., Moore, B., Governato, F., Lake, G., Quinn, T., & Stadel, J. 1998, MNRAS, 300, 146
Gnedin, O. Y., Kravtsov, A. V., Klypin, A. A., & Nagai, D. 2004, ApJ, 616, 16
Griffiths, R. E., Casertano, S., Im, M., & Ratnatunga, K. U. 1996, MNRAS, 282, 1159
Guzik, J., & Seljak, U. 2002, MNRAS, 335, 311
Hayashi, E., Navarro, J. F., & Springel, V. 2007, MNRAS, 377, 50
Heymans, C., et al. 2006a, MNRAS, 368, 1323
———. 2006b, MNRAS, 371, L60
Hoekstra, H., Franx, M., Kuijken, K., & Squires, G. 1998, ApJ, 504, 636
Hoekstra, H., Hsieh, B. C., Yee, H. K. C., Lin, H., & Gladders, M. D. 2005, ApJ, 635, 73
Hoekstra, H., Yee, H. K. C., & Gladders, M. D. 2004, ApJ, 606, 67
Humphrey, P. J., Buote, D. A., Gastaldello, F., Zappacosta, L., Bullock, J. S., Brighenti, F., & Mathews, W. G. 2006, ApJ, 646, 899
Jing, Y. P. 2000, ApJ, 535, 30
———. 2002, MNRAS, 335, L89
Kaiser, N., & Squires, G. 1993, ApJ, 404, 441
Kaiser, N., Squires, G., & Broadhurst, T. 1995, ApJ, 449, 460
Kazantzidis, S., Kravtsov, A. V., Zentner, A. R., Allgood, B., Nagai, D., & Moore, B. 2004, ApJ, 611, L73
Keeton, C. R. 2001, preprint (astro-ph/0102341)
Keeton, C. R., & Zabludoff, A. I. 2004, ApJ, 612, 660
Kleinheinrich, M., et al. 2006, A&A, 455, 441
Kneib, J.-P., et al. 2003, ApJ, 598, 804
Kochanek, C. S. 1995, ApJ, 445, 559
Koekemoer, A. M., Fruchter, A. S., Hook, R. N., & Hack, W. 2002, in The 2002 *HST* Calibration Workshop: Hubble after the Installation of the ACS and the NICMOS Cooling System, ed. S. Arribas, A. Koekemoer, & B. Whitmore (Baltimore, STScI), 337
Koopmans, L. V. E., & Treu, T. 2002, ApJ, 568, L5
———. 2003, ApJ, 583, 606
Koopmans, L. V. E., Treu, T., Bolton, A. S., Burles, S., & Moustakas, L. A. 2006, ApJ, 649, 599 (Paper III)
Krist, J., & Hook, R. 2004, The TinyTim Users Manual (Baltimore: STScI)
Kronawitter, A., Saglia, R. P., Gerhard, O., & Bender, R. 2000, A&AS, 144, 53
Leauthaud, A., et al. 2007, ApJS, 172, 219
Limousin, M., et al. 2006, ApJ, submitted (astro-ph/0612165)
Mamon, G. A., & Łokas, E. L. 2005a, MNRAS, 362, 95
———. 2005b, MNRAS, 363, 705
Mandelbaum, R., Seljak, U., Kauffmann, G., Hirata, C. M., & Brinkmann, J. 2006, MNRAS, 368, 715 (M06)
Mandelbaum, R., Tasitsiomi, A., Seljak, U., Kravtsov, A. V., & Wechsler, R. H. 2005, MNRAS, 362, 1451
Maoz, D., & Rix, H. 1993, ApJ, 416, 425
Massey, R., et al. 2007, MNRAS, 376, 13
Mellier, Y. 1999, ARA&A, 37, 127
Merrett, H. R., et al. 2006, MNRAS, 369, 120
Moore, B., Ghigna, S., Governato, F., Lake, G., Quinn, T., Stadel, J., & Tozzi, P. 1999, ApJ, 524, L19
Moore, B., Governato, F., Quinn, T., Stadel, J., & Lake, G. 1998, ApJ, 499, L5
Natarajan, P., & Kneib, J.-P. 1997, MNRAS, 287, 833
Natarajan, P., Kneib, J.-P., & Smail, I. 2002, ApJ, 580, L11
Navarro, J. F., Frenk, C. S., & White, S. D. M. 1997, ApJ, 490, 493
Navarro, J. F., et al. 2004, MNRAS, 349, 1039

Peng, C. Y., Ho, L. C., Impey, C. D., & Rix, H. 2002, AJ, 124, 266
Rhodes, J. D., et al. 2007, ApJS, in press (astro-ph/0702140) (R07)
Romanowsky, A. J., Douglas, N. G., Arnaboldi, M., Kuijken, K., Merrifield, M. R., Napolitano, N. R., Capaccioli, M., & Freeman, K. C. 2003, Science, 301, 1696
Rusin, D., & Kochanek, C. S. 2005, ApJ, 623, 666
Rusin, D., Kochanek, C. S., & Keeton, C. R. 2003, ApJ, 595, 29
Salucci, P. 2001, MNRAS, 320, L1
Sand, D. J., Treu, T., Smith, G. P., & Ellis, R. S. 2004, ApJ, 604, 88
Schlegel, D. J., Finkbeiner, D. P., & Davis, M. 1998, ApJ, 500, 525
Schneider, P. 2006, in Gravitational Lensing: Strong, Weak and Micro, ed. G. Meylan et al. (Berlin: Springer), 1
Schrabback, T., et al. 2007, A&A, in press (astro-ph/0606611)
Seljak, U., et al. 2005, Phys. Rev. D, 71, 103515
Sheldon, E. S., et al. 2004, AJ, 127, 2544 (S04)
Simon, J. D., Bolatto, A. D., Leroy, A., Blitz, L., & Gates, E. L. 2005, ApJ, 621, 757
Spergel, D. N., et al. 2007, ApJS, 170, 377
Stoehr, F., White, S. D. M., Tormen, G., & Springel, V. 2002, MNRAS, 335, L84
Swaters, R. A., Madore, B. F., van den Bosch, F. C., & Balcells, M. 2003, ApJ, 583, 732
Taylor, J. E., & Babul, A. 2004, MNRAS, 348, 811
Tegmark, M., et al. 2004, ApJ, 606, 702
Treu, T., & Koopmans, L. V. E. 2002, ApJ, 575, 87
———. 2004, ApJ, 611, 739
Treu, T., Koopmans, L. V. E., Bolton, A. S., Burles, S., & Moustakas, L. A. 2006a, ApJ, 640, 662 (Paper II)
———. 2006b, ApJ, 650, 1219
Treu, T., Stiavelli, M., Bertin, G., Casertano, S., & Møller, P. 2001, MNRAS, 326, 237
Treu, T., et al. 2005, ApJ, 633, 174
Trujillo, I., Burkert, A., & Bell, E. F. 2004, ApJ, 600, L39
van der Wel, A., Franx, M., van Dokkum, P. G., Rix, H.-W., Illingworth, G. D., & Rosati, P. 2005, ApJ, 631, 145
Wilson, G., Kaiser, N., Luppino, G. A., & Cowie, L. L. 2001, ApJ, 555, 572
Wright, C. O., & Brainerd, T. G. 2000, ApJ, 534, 34